High-resolution induced polarization imaging of biogeochemical carbon turnover hot spots in a peatland

Timea Katona[1], Benjamin Silas Gilfedder[2], Sven Frei[2], Matthias Bücker[3], and Adrian Flores-Orozco[1]

(1) Research Division Geophysics, Department of Geodesy and Geoinformation, TU-Wien, Austria;

(2) Department of Hydrology, University of Bayreuth, Germany;

(3) Institute for Geophysics and Extraterrestrial Physics, TU Braunschweig, Germany

Abstract

Biogeochemical hot spots are defined as areas where biogeochemical processes occur with anomalously high reaction rates relative to their surroundings. Due to their importance in carbon and nutrient cycling, the characterization of hot spots is critical to predicting carbon budgets accurately in the context of climate change. However, biogeochemical hot spots are difficult to identify in the environment, as methods for in-situ measurements often directly affect the sensitive redox-chemical conditions. Here, we present imaging results of a geophysical survey using the non-invasive induced polarization (IP) method to identify biogeochemical hot spots of carbon turnover in a minerotrophic wetland. To interpret the field-scale IP signatures, geochemical analyses were performed on freeze-core samples obtained in areas characterized by anomalously high and low IP responses. Our results reveal large variations in the electrical response, with the highest IP phase values (> 18 mrad) corresponding with high concentrations of phosphates (>4000 µM), an indicator of carbon turnover. Furthermore, we found a strong relationship between the electrical properties resolved in IP images and the dissolved organic carbon. Moreover, analysis of the freeze core reveals negligible concentrations of iron sulfides. The extensive geochemical and geophysical data presented in our study demonstrates that IP images can track small scale changes in the biogeochemical activity in peat and can be used to identify hot spots.

Keywords: biogeochemical carbon turnover; geophysical imaging methods; electrical conductivity; induced polarization; microbiologically active zones

1 Introduction

In terrestrial and aquatic ecosystems, patches or areas that show disproportionally high biogeochemical reaction rates relative to the surrounding matrix are referred to as biogeochemical 'hot spots' (McClain et al., 2003). Hot spots for turnover of redox-sensitive species (e.g., oxygen, nitrate or dissolved organic carbon) are often generated at interfaces between oxic and anoxic environments, where the local presence/absence of oxygen either favors or suppresses biogeochemical reactions such as aerobic respiration, denitrification, or oxidation/reduction of iron (McClain et al., 2003). Biogeochemical hot spots are important for nutrient and carbon cycling in various systems such as wetlands (Frei et al., 2010; 2012), lake sediments (Urban, 1994), the vadose zone (Hansen et al., 2014), hyporheic areas (Boano et al., 2014) or aquifers (Gu et al., 1998). Wetlands are distinct elements in the landscape, which are often located where hydrological flow paths converge, such as at the bottoms of basin shaped catchments, local depressions or around rivers and streams (Cirmo and McDonell 1997). Wetlands are attracting increasing interest because of their important contribution to water supply, water quality, nutrient cycling, and biodiversity (Costanza et al., 1997; 2017). Understanding microbial moderated cycling of nutrients and carbon in wetlands is critical, as these systems store a significant part of the global carbon through the accumulation of decomposed plant material (Kayranli et al., 2010). In wetlands, water table fluctuations as well as plant roots determine the vertical and horizontal distribution of oxic and anoxic areas (Frei et al., 2012; Gutknecht et al., 2006). Small scale subsurface flow processes in wetlands, moderated by micro-topographical structures (hollow and hummocks) (Diamond et al., 2020), can control the spatial presence of redox-sensitive solutes and formation of biogeochemical hot spots (Frei et al., 2010; 2012). Despite their relevance for the carbon and nutrient cycling, basic mechanisms controlling the formation and distribution of biogeochemical hot spots in space are not well understood.

Biogeochemical active areas traditionally have been identified and localized through chemical analyses of point samples from the subsurface and subsequent interpolation of the data in space (Morse et al., 2014; Capps and Flecker, 2013; Hartley and Schlesinger, 2000). However, such point-based sampling methods may either miss hot spots due to the low spatial resolution of sampling (McClain et al., 2003) or disturb the redox-sensitive conditions in the subsurface by bringing oxygen into anoxic areas during sampling. Non-invasive methods, such as geophysical techniques, have the potential to study subsurface biogeochemical activity in-situ without interfering with the subsurface environment (e.g., Williams et al., 2005; 2009; Atekwana and Slater 2009; Flores Orozco et al., 2015; 2019; 2020). Geophysical methods permit to map large

65 areas in 3D and still resolve subsurface physical properties with a high spatial resolution (Binley

66 et al., 2015).

67 In particular, the induced polarization (IP) technique has recently emerged as a useful tool to

68 delineate biogeochemical processes in the subsurface (e.g., Kemna et al., 2012; Kessouri et al.,

69 2019; Flores Orozco et al., 2020). The IP method provides information about the electrical

70 conductivity and the capacitive properties of the ground, which can be expressed, respectively,

71 in terms of the real and imaginary components of the complex resistivity (Binley and Kemna,

72 2005). The method is commonly used to explore metallic ores because of the strong polarization

73 response associated with metallic minerals (e.g., Marshall and Madden, 1959; Seigel et al.,

74 2007). Pelton et al. (1978) and Wong (1979) proposed the first models linking the IP response

75 to the size and content of metallic minerals. More recently, the role of chemical and textural

76 properties in the polarization of metallic minerals has been investigated in detail based on

77 further developments of Wong's model of a perfect conductor and reaction currents (Bücker et

78 al., 2018; 2019); while Revil et al. (2012, 2015a, 2015b, 2017b, 2017c, 2018) have presented a

79 new mechanistic model that takes into account the intragrain polarization and Feng et al. (2020)

80 have explained the polarization of perfectly conducting particles based on a Stern-layer

81 capacitance. The two latter groups of models do not involve reaction currents. In porous media

82 without a significant metallic content, the IP response can be related to the polarization of the

83 electrical double layer formed at the grain-fluid interface (e.g., Revil and Florsch, 2010; Revil,

84 2012). For instance, Revil et al. (2017a) carried out IP measurements on a large set of soil

85 samples, for which they report a linear relationship between the magnitude of the polarization

86 response and the cation exchange capacity (CEC), which is related to surface area and surface

87 charge density.

88 Since the early 2010s, various studies have explored the potential of IP measurement for the

89 investigation of biogeochemical processes in the emerging field of biogeophysics (Slater and

90 Attekwana, 2013). Laboratory studies on sediment samples examined the correlation between

91 the spectral induced polarization (SIP) response and iron sulfide precipitation caused by iron

92 reducing bacteria (Williams et al., 2005; Ntarlagiannis et al., 2005; 2010; Slater et al., 2007;

93 Personna et al., 2008; Zhang et al., 2010; Placencia Gomez et al., 2013; Abdel Aal et al., 2014).

94 Further investigations in the laboratory have also revealed an increase in the polarization

95 response accompanying the accumulation of microbial cells and biofilms (Davis et al., 2006;

96 Abdel Aal et al., 2010a, 2010b; Albrecht et al., 2011; Revil et al., 2012; Zhang et al., 2013;

97 Mellage et al., 2018; Rosier et al., 2019; Kessouri et al., 2019).

Motivated by these observations, the IP method has also been used to characterize biogeochemical degradation of contaminants at the field scale (Williams et al., 2009; Flores Orozco et al., 2011; 2012b; 2013; 2015; Maurya et al., 2017). Additionally, Wainwright et al. (2016) demonstrated the applicability of the IP imaging method to identify naturally reduced zones, i.e., hot spots, at the floodplain scale. These authors show that the accumulation of organic matter in areas with indigenous iron-reducing bacteria results in naturally reduced zones and the accumulation of iron sulfide minerals, which are classical IP targets. In line with this argumentation, Abdel Aal and Atekwana (2014) argued that the biogeochemical precipitation of iron sulfides control the high electrical conductivity and IP response observed in hydrocarbon-impacted sites. Nonetheless, in a recent study, Flores Orozco et al. (2020) demonstrated the possibility to delineate biogeochemically active zones in a municipal solid waste landfill even in the absence of iron sulfides. Flores Orozco et al. (2020) argued that the high content of organic matter itself might explain both, the high polarization response and high rates of microbial activity; thus, opening the possibility to delineate biogeochemical hot spots that are not related to iron-reducing bacteria. This conclusion is consistent with previous studies performed in marsh and peat soils, areas with a high organic matter content and high microbial turnover rates (Mansoor and Slater, 2007; McAnallen et al., 2018). Peat soils are characterized by a high surface charge and have been suggested to enhance the IP response (Slater and Reeve, 2002). Mansoor and Slater (2007) concluded that the IP method is a useful tool to map iron cycling and microbial activity in marsh soils. Garcia-Artigas et al. (2020) demonstrated that bioclogging by bacteria increases the IP response accompanying wetlands treatment. Uhlemann et al. (2016) found differences in the electrical resistivity of peat according to saturation, microbial activity, and pore water conductivity; however, their study was limited to direct-current resistivity and did not investigate variations in the IP response. In contrast to these observations, laboratory studies have shown a low polarization response in samples with a high organic matter content, despite its high CEC (Schwartz and Furman, 2014). Based on field measurements, McAnallen et al. (2018) found that active peat is less polarizable due to variations in groundwater chemistry imposed by sphagnum mosses; while degrading peat resulted in low resistivity values and a high polarization response. Based on measurements with the Fourier Transform Infrared (FTIR) Spectroscopy in water samples, the authors concluded that the carbon-oxygen (C=O) double-bond in degrading peat correlated with the polarization magnitude of the peat material. Based on laboratory investigations, Ponziani et al. (2011) also conclude that decomposition of peat occurs predominantly by aerobic respiration, i.e. using molecular oxygen as the terminal electron acceptor to oxidize organic matter. Thus

132 decomposition rates are expected to be highest at the interface between the oxic and anoxic
133 zones.

134 Based on these promising previous results, we hypothesize that the IP method is a potentially
135 useful tool for in-situ investigation of biogeochemical processes and the mapping of
136 biogeochemical hot spots. However, different responses observed in lab and field investigations
137 do not offer a clear interpretation scheme of general validity. Additionally, it is not clear
138 whether the IP method is only suited to characterize biogeochemical hot spots associated to
139 iron-reducing bacteria, which favor the accumulation of iron sulfides. Hence, in this study we
140 present an extensive IP imaging dataset collected at a peatland site to investigate the controls
141 on the IP response in biogeochemically active areas. IP monitoring results are compared to
142 geochemical data obtained from the analysis of freeze cores and pore water samples. Our main
143 objectives are (i) to assess the applicability of the IP method to spatially delimit highly active
144 biogeochemical areas in the peat soil and (ii) to investigate whether the local IP response is
145 related to the accumulation of iron sulfides or high organic matter turnover.

2 Material and methods

146

147 2.1 Study site

148 The study site is part of the Lehstenbach catchment located in the Fichtelgebirge mountains
149 (Fig. 1a), a low mountain range in north-eastern Bavaria (Germany) close to the border to the
150 Czech Republic. Various soil types including Dystric Cambisols, Haplic Podsols, and Histosols
151 (i.e. peat soil) cover the catchment area of approximately 4.2 km², situated on-top of variscan
152 granite bedrock (Strohmeier et al., 2013). The catchment is bowl shaped (Fig. 1b), and
153 minerotrophic riparian peatlands have developed around the major streams. The plot scale study
154 site (Fig. 1c) is located in a riparian peatland draining into a nearby stream close to the
155 'catchment's outlet (Fig. 1b).

156 The groundwater level in this area annually varies within the top 30 cm of the peat soil, and the
157 local groundwater flow has a S-SW orientation (Durejka et al., 2019) towards a nearby drainage
158 ditch. Permanently high water saturation of the peat soil favors the development of anoxic
159 biogeochemical processes close to the surface. Frei et al. (2012) demonstrated that hot spots at
160 the study area are related to the stimulation of iron reducing bacteria and accumulation of iron
161 sulfides, which are generated by small scale subsurface flow processes and the spatial non
162 uniform availability of electron acceptors and donors induced by the typical micro topography
163 of the peatland. Non uniform availability of electron acceptors and donors in combination with

164 labile carbon stocks are the primary drivers in generating biogeochemical hot spots in the
165 peatland (Frei et al., 2012; Mishra and Riley, 2015).

166 2.2 Experimental plot and geochemical measurements

167 The experimental plot for the geophysical measurements covers approximately 160 m² (12.6 x
168 12.6 m, Fig. 1c) of the riparian peatland. Sphagnum Sp. (peat moss) and Molinia caerulea
169 (purple moor-grass) dominate the vegetation, with the sphagnum and purple moor-grass
170 abundance being higher in the Northern part of the plot (Fig. 2a and 2b). In the Southeastern
171 region, where the sphagnum is less abundant, permanent surface runoff was observed (Fig. 2d).
172 Peat thickness was measured with a 1 m resolution in E-W direction and 0.5 m resolution in N-
173 S direction (along the IP profiles described below). To measure the thickness of the peat, a
174 stainless-steel rod (0.5 cm in diameter) was pushed into the ground until it reached the granitic
175 bedrock (similar to Parry et al., 2014). The local groundwater level was measured in two
176 piezometers and was found at ~5-8 cm below the surface during the IP survey. Groundwater
177 samples were collected at three different locations (S1, S2, and S3 indicated in Fig. 3) using a
178 bailer. Pore water profiles were taken at S1, S2, and S3 at 5 cm intervals to a maximum depth
179 of 50 cm below ground surface (bgs) using stainless steel mini-piezometers. All water samples
180 were filtered through 0.45 µm filters and analyzed for fluoride, chloride, nitrite, bromide,
181 nitrate, phosphate, and sulfate using an ion chromatograph (Compact IC plus 882, Metrohm
182 GMBH). Dissolved organic carbon (DOC) was measured using a Shimadsu TOC analyzer via
183 thermal combustion. Dissolved iron species (Fe^{2+}) and total iron (Fe^{tot}) concentrations were
184 measured photometrically using the 1,10-phenanthroline method on pore water samples that
185 had been stabilized with 1% vol/vol 1M HCl in the field (Tamura et al., 1974). Two freeze cores
186 (see Fig. 2d) were extracted at locations S1 and S2 (Fig. 3) by pushing an 80-cm long stainless-
187 steel tube into the peat. After the tube was installed, it was filled with a mixture of dry ice and
188 ethanol. After around 20 minutes, the pipe with the frozen peat sample was extracted and stored
189 on dry ice for transportation to the laboratory at the University of Bayreuth. Both freeze cores
190 were cut into 10 cm segments. Each segment was analyzed for reactive iron (1M HCl extraction
191 and measured for Fe^{tot} as described above) (Canfield, 1989), reduced sulfur species using the
192 total reduced inorganic sulfur (TRIS) method (Canfield et al., 1986) and carbon and nitrogen
193 concentrations after combustion using a thermal conductivity detector. Peat samples were also
194 analyzed by FTIR using a Vector 22 FTIR spectrometer (Bruker, Germany) in absorption mode;
195 with subsequent baseline subtraction on KBr pellets (200 mg dried KBr and 2 mg sample).
196 Thirty-two measurements were recorded per sample and averaged from 4.500 to 600 cm^{-1} in a
197 similar manner to Biester et al. (2014).

2.3 Non-invasive techniques: induced polarization measurements

The induced polarization (IP) imaging method, also known as complex conductivity imaging or electrical impedance tomography, is an extension of the electrical resistivity tomography (ERT) method (e.g., Kemna et al., 2012). As such, it is based on four-electrode measurements, where one pair of electrodes is used to inject a current (current dipole) and a second pair of electrodes is used to measure the resulting electrical potential (potential dipole). Modern devices can measure tens of potential dipoles simultaneously for a given current dipole, permitting the collection of dense data sets within a reasonable measuring time. This provides an imaging framework to gain information about lateral and vertical changes in the electrical properties of the subsurface. IP data can be collected in the frequency domain (FD), where an alternating current is injected into the ground where the polarization of the ground leads to a measurable phase shift between the injected periodic current and the measured voltage signals. From the ratio of the magnitudes of the measured voltage and the injected current, as well as the phase shift between the two signals, we can obtain the electrical transfer impedance. The inversion of imaging data sets, i.e. a large set of such four-point transfer-impedance measurements collected at different locations and with different spacing between electrodes along a profile, permits to solve for the spatial distribution of the electrical properties in the subsurface (see deGroot-Hedlin and Constable, 1990; Kemna et al., 2000; Binley and Kemna, 2005).

IP inversion results can be expressed in terms of the complex conductivity (σ^*) or its inverse the complex resistivity ($\sigma^*=1/\rho^*$). The complex conductivity can either be denoted in terms of its real (σ') and imaginary (σ'') components, or in terms of its magnitude ($|\sigma|$) and phase (φ):

$$\sigma^*=\sigma'+i\sigma'' =|\sigma|e^{i\phi}, \qquad (1)$$

where $i = \sqrt{-1}$ is the imaginary unit, $|\sigma| = \sqrt{\sigma'^2 + \sigma''^2}$ and $\phi =\tan^{-1}(\sigma'/\sigma'')$. The real part of the complex conductivity is mainly related to the Ohmic conduction, while the imaginary part is mainly related to the polarization of the subsurface. The conductivity (σ') is related to porosity, saturation, the conductivity of the fluid filling the pores and a contribution of the surface conductivity (Lesmes and Frye, 2001). The polarization (σ'') is only related to the surface conductivity taking place at the electrical double layer (EDL) at the grain-fluid interface. For a detailed description of the IP method, the reader is referred to the work of Ward (1988), Binley and Kemna (2005), and Binley and Slater (2020).

The strongest polarization response is observed in the presence of electrically conducting minerals (e.g., iron) (e.g., Pelton et al., 1978) in the so-called electrode polarization (Wong et al., 1979). It arises from the different charge transport mechanisms in the electrical conductor

(electronic or semiconductor conductivity) and the electrolytic conductivity of the surrounding pore fluid, which make the solid-liquid interface polarizable. Diffusion-controlled charging and relaxation processes inside the grain (e.g., Revil et al., 2018; 2019; Abdulsamad et al., 2020) or outside the grain in the electrolyte (e.g., Wong, 1979; Bücker et al., 2019) are considered as possible causes of the polarization response at low frequencies irrespective of the specific modeling approach. All mechanistic models predict an increase in the polarization response with increasing volume content of the conductive minerals (Wong, 1979; Revil et al. 2015a, 2015b, 2017a, 2017b, 2018; Qi et al., 2018; Bücker et al., 2018).

In the absence of electron conductors, the polarization response is only related to the accumulation and polarization of ions in the EDL. Different models have been proposed to describe the polarization response as a function of grain size, surface area and surface charge (e.g., Schwarz, 1962; Schurr, 1964; Leroy et al., 2008). Alternatively, the membrane polarization related the IP response to variations in the geometry of the pores as well as the concentration and mobility of the ions (e.g., Marshall and Madden, 1959; Bücker and Hördt, 2013; Bücker et al., 2019). Regardless of the specific modeling approach, EDL polarization mechanisms strongly depend on the specific surface area of the material and the charge density at the surface (Revil, 2012; Waxman and Smits, 1968).

In this study, we conducted FDIP measurements at 1 Hz along 65 lines during a period of four days in July 2019. We used the DAS-1 instrument manufactured by Multi-Phase Technologies (now MTP-IRIS Inc.). We collected 64 N-S oriented lines (referred to as By 1 to By 64) with 20 cm spacing between each line. One additional line (By 68) was collected with a W-E orientation, which intersects the N-S oriented lines at 3 m, as presented in Fig. 3. Each profile consisted of 64 stainless steel electrodes (3 mm diameter) with a separation of 20 cm between each electrode (Fig. 2c). Besides the short electrode spacing, the use of a dipole-dipole configuration with a unit dipole length of 20 cm warranted a high resolution within the upper 50 cm of the peat, where the biogeochemical hot spots were expected. We deployed a dipole-dipole skip-0 (i.e., the dipole length for each measurement is equal to the unit spacing of 20 cm) configuration; voltage measurements were collected across eight adjacent potential dipoles for each current dipole. The dipole-dipole configuration avoids the use of electrodes for potential measurements previously used for current injections to avoid contamination of the data caused by remnant polarization of electrodes. To evaluate data quality, reciprocal readings were collected along one profile every day (see, e.g., LaBrecque et al., 1996; Flores Orozco et al., 2012a; 2019). Reciprocal readings refer to data collected after interchanging current and

265 potential dipoles. We used coaxial cables to connect the electrodes with the measuring device

266 to minimize the distortion of the data due to electromagnetic coupling and cross-talking

267 between the cables (e.g., Zimmermann et al., 2008, 2019; Flores Orozco et al., 2013), with the

268 shields of all coaxial cable running together into one ground electrode (for further details see

269 Flores Orozco et al., 2021).

270 The principle of reciprocity asserts that normal and reciprocal readings should be the same (e.g.,

271 Slater et al., 2000). Hence, we use here the analysis of the discrepancy between normal and

272 reciprocal readings to detect outliers and to quantify data error (LaBrecque et al., 1996; Flores

273 Orozco et al., 2012a; Slater and Binley, 2006; Slater et al., 2000). In this study, we quantified

274 the error parameter for each line collected as normal and reciprocal pairs (using the approach

275 outlined by Flores Orozco et al., 2012a) and computed the average value of the error parameters

276 for the different lines to define the error model used for the inversion of all imaging data sets.

277 For the inversion of the IP imaging data set, we used CRTomo, a smoothness-constrained least-

278 squares algorithm by Kemna (2000) that allows inversion of the data to a level of confidence

279 specified by an error model. We used the resistance and phase error models described by Kemna

280 (2000) and Flores Orozco et al. (2012a). The resistance (R) error model is expressed as

281 $s(R)=a+bR$, where a is the absolute error, which dominates at small resistances (i.e., $R < 0$),

282 and b is the relative error, which dominates at high resistance values (LaBrecque et al., 1996;

283 Slater et al., 2000). For the phase, the error model is also expressed as a function of the

284 resistance $s(\phi_a)=cR^d$, where $d<0$ in our study due to the relatively low range in the measured

285 resistances (see Flores Orozco et al., 2012a for further details). If $d{\rightarrow}0$, the model reduces to

286 the constant-phase-error model (Flores Orozco et al., 2012a) with $s(\phi)=c$ described by Kemna

287 (2000) and Slater and Binley (2006).

3 Results

288

289 3.1 Data quality and processing

290 In Fig. 4, we present a modified pseudosection showing both normal (negative pseudodepth)

291 and reciprocal (positive pseudodepth) readings in terms of apparent resistivity (ρ_a) and apparent

292 phase (ϕ_a) for the data collected along line By 25. Plots in Fig. 4 show consistency between the

293 normal and reciprocal readings of apparent resistivity (4a) and phase (4b). Figures 4c and 4d

294 show the histograms of the normal-reciprocal misfits along line By 25 for both the resistance

295 and phase (ΔR and $\Delta \phi$ respectively), which exhibit near Gaussian distributions with low

296   standard deviations (as expected for random noise) for both the normalized resistance

297   (S_R=0.027) and the apparent phase (S_ϕ=1.1 mrad). Readings exceeding these standard deviation

298   values were considered as outliers (between 16 and 33% of the data at the different lines) and

299   were removed from the data set prior to the inversion.

300   Here, we present inversion results obtained using the error parameters, $a = 0.001\ \Omega$, $b = 0.022$,

301   and $c = 1$ mrad. For the imaging, we defined a cut-off value of the cumulated sensitivity of

302    $10^{2.75}$, with pixels related to a lower cumulated sensitivity blanked in the images. The cumulated

303   sensitivity values are a widely used parameter to assess the depth of investigation (Kemna et

304   al., 2002; Flores Orozco et al., 2013).

305   3.2 Complex conductivity imaging results and their link to the peat thickness and land

306   cover

307   The thickness of the peat in the plot was found to vary between 40 and 160 cm (Fig. 5). The

308   thickness of the peat unit increased in the W-E direction, with much smaller variations in the

309   N-S direction. Variations in the vegetation cover (as indicated by the three vegetation classes,

310   abundant (*av*), moderate (*mv*), and sparse (*sv*)) do not seem to correspond with the variations in

311   the peat thickness. Note that the N-S orientation of the majority of IP lines is approximately

312   aligned with the direction of minimum changes in the peat thickness.

313   Figure 6 shows the imaging results of the N-S oriented profiles By 25, By 46, and the W-E

314   oriented profile By 68 expressed in terms of the conductivity (σ') and polarization (σ''). These

315   images reveal three main electrical units: (i) a shallow peat unit with high σ' (>5 mSm^{-1}) and

316   high σ'' (>100 μSm^{-1}) values in the top 10-20 cm bgs, (ii) an intermediate unit in the peat with

317   moderate to low 'σ' (<5 mSm^{-1}) and moderate σ'' (40– 100 μSm^{-1}) values, and (iii) underneath

318   it, a third unit characterized by moderate to low σ' (<5 mSm^{-1}) and the lowest σ'' (<40 μSm^{-1})

319   values corresponding to the granite bedrock. The compact structure of the granite,

320   corresponding to low porosity, explains the observed low conductivity values (σ' <5 mSm^{-1})

321   due to low surface charge and surface area. The shallow and intermediate electrical units are

322   related to the relatively heterogeneous peat (Fig. 6), which is beyond the vertical change and

323   lateral heterogeneities in the complex conductivity parameters. As shown in the plots of σ'' in

324   Fig. 6, the contact between the second and third unit roughly corresponds to the contact between

325   peat and granite measured with the metal rod. This indicates the ability of IP imaging to resolve

326   the geometry of the peat unit. However, for the survey design used in this study, σ'' images are

327   not sensitive to materials deeper than ~1.25 m. Images of the electrical conductivity reveal

much more considerable variability and a lack of clear contrasts between the peat and the granite materials, likely due to the weathering of the shallow granite unit (Lischeid et al., 2002, Partington et al., 2013).

The phase of the complex conductivity represents the ratio of the polarization relative to the Ohmic conduction ($\phi = \sigma''/\sigma'$). Thus, it can also be used to represent the polarization response (Kemna et al., 2004; Ulrich and Slater 2004; Flores Orozco et al., 2020). Similar to the σ'' images, the phase images presented in Fig. 7 resolve the three main units: (i) the shallow peat unit within the top 10-50 cm is characterized by the highest values ($\phi > 18$ mrad), (ii) the intermediate unit still corresponding to peat, is characterized by moderate ϕ values (between 13 and 18 mrad), and (3) the third unit, associated to the granitic bedrock, related to the lowest ϕ values (< 13 mrad). The polarization images expressed in terms of ϕ show a higher contrast between the peat and the granite units than the σ' (or σ'') images. The histograms presented in Fig. 7 show the distribution of the phase values in the images, with a different color for model parameters extracted above and below the contact between peat and granite. The histograms highlight that the lowest phase values clearly correspond to the granite bedrock (< 13 mrad), while higher phase values are characteristic of the peat unit.

Moreover, the shallow unit shows more pronounced lateral variations in the phase than in σ'', and patterns within the peat unit are more clearly defined. As observed in Fig. 6, along line By 25, the thickness of the first unit decreases from approx. 0.5 m at 2 m along the profile to 0 m around 10 m at the end of the profile. Along line By 46, the first unit is slightly thicker than 50 cm and shows the highest phase values (~25 mrad) between 0 and 6.5 m along the profile. Beyond 6.5 m, the polarizable unit becomes discontinuous with isolated polarizable (~18 mrad) zones, extending to a depth of 50 cm. The geometry of the shallow, polarizable unit is consistent with the corresponding results along line By 68, which crosses By 25 and By 46 at 3 m along these lines (S1 and S3 are located at these intersections). In particular, the highest phase values are consistently found in the shallowest 50 cm in the peat unit, at the depth where biogeochemical hot spots have been reported in the study by Frei et al. (2012).

Figure 8 presents maps of the electrical parameters at different depths aiming to identify lateral changes in the possible hot spots across the entire experimental plot. Such maps present the interpolation of values inverted in each profile. Along each profile, a value is obtained through the average of model parameters (conductivity magnitude and phase) within the surface and a depth of 20 cm (shallow maps) and between 100 and 120 cm (for deep maps). The western part of the experimental plot (between 0 and 4 m in X-direction and between 2 and 9 m in Y-

361 direction) corresponds to a shallow depth to the bedrock (a peat thickness of ~ 50-70 cm) and

362 is associated with high electrical parameters in the shallow maps (ϕ >18 mrad, σ'>7 mSm^{-1} and

363 σ''>100 μSm^{-1}), which we can interpret here as the geometry of the biogeochemical hot spots.

364 Another hot spot can be identified in the Northern part of the experimental plot, in the area with

365 abundant vegetation; we observe a higher polarization response for the top 20 cm (ϕ>18 mrad

366 and σ''>80 μSm^{-1}) than, for instance, the one corresponding to the moderate vegetation located

367 at the southern part. In contrast, the lowest polarization values (ϕ <15 mrad, and σ'' <80 μSm^{-1})

368 values, which we interpret as biogeochemical inactive zones, are related to the area with sparse

369 vegetation and permanent surface runoff.

370 Kleinebecker et al. (2009) suggest that besides climatic variables, biogeochemical

371 characteristics of the peat influence the composition of vegetation in wetlands. Hence, we can

372 use variations in the vegetation as a qualitative way to evaluate our interpretation of the IP

373 imaging results. In Fig. 8j to 8l, we present the histograms of the electrical parameters extracted

374 at each of the three vegetation features defined in the experimental plot (abundant, moderate

375 and sparse). These histograms show, in general, that the location with sparse vegetation, i.e.,

376 with permanent surface runoff, is related to the lowest phase values (histogram peak at 13

377 mrad). Moderate vegetation corresponds with moderate phase and σ'' values (histogram peak at

378 18 mrad and 70 μSm^{-1}, respectively). In comparison, the abundant vegetation corresponds with

379 the highest phase and σ'' values (histogram peak at 22 mrad and 90 μSm^{-1}, respectively) in the

380 top 20 cm. The histogram of the three vegetation features in terms of σ' values overlaps with

381 each other.

382 3.3 Comparison of electrical and geochemical parameters

383 The evaluation of the imaging results measured along profiles By 25, By 46, and By 68 were

384 used to select the locations for the freeze core and sampling of groundwater. Sampling points

385 S1 and S3 were defined in the highly polarizable parts of the uppermost peat unit (high σ' and

386 σ'' values). In contrast, sampling point S2 is located in an area characterized by low polarization

387 values. Figures 9a-e show the chemical parameters measured in the water samples, specifically

388 chloride (Cl$^-$), phosphate (PO$_4^{3-}$), dissolved organic carbon (DOC), total iron (Fe$_{tot}$ = Fe^{2+} +

389 Fe^{3+}), and pH; whereas Fig. 9f-j show the chemical parameters measured in the peat samples

390 extracted from the freeze cores, namely, cation exchange capacity (CEC), concentrations of

391 iron sulfide (FeS or FeS$_2$), total reactive iron (Fe$_{tot}$), potassium (K$^+$), and sodium (Na$^+$). The

392 pore-fluid conductivity measured in water samples retrieved from the piezometers shows minor

393 variation with values ranging between 6.7 and 10.4 mSm^{-1}.To facilitate the comparison of

394   electrical parameters and geochemical data, Fig. 9k-m show the complex conductivity

395   parameters (σ', σ'' and ϕ) at the sampling points S1, S2 and S3, which were extracted as vertical

396   1D profiles from the corresponding imaging results.

397   As observed in Fig. 6 and 7, the highest complex conductivity values (σ', σ'') were resolved

398   within the uppermost 10-20 cm and rapidly decreased with depth. Furthermore, the values of ϕ

399   and σ'' in the top 20 cm at S1 and S3 are significantly higher than those at the location S2. High

400   values of ϕ and σ'' at S1 and S3 correspond with high concentrations of DOC, phosphate$^-$, Fe_{tot}

401   in water samples, as well as with high K^+, and Na^+ contents measured in soil materials extracted

402   from the freeze cores. Figure 9 reveals consistent patterns between geochemical and

403   geophysical parameters: in the first 10 cm bgs close to the sampling points S1 and S3, we

404   observe complex conductivity values (σ' and σ'') as well as chemical parameters, such as DOC,

405   phosphate (only at S1). Accordingly, as S1 Fe_{tot} also reveals at least two times higher

406   concentrations than those measured in S2.

407   Figure 10 shows the actual correlations between the complex conductivity and Cl^-, DOC, and

408   Fe_{tot} concentrations measured in groundwater samples. In Fig. 10, we also provide a linear

409   regression analysis to quantify the correlation between parameters. Figure 10 reveals that the

410   phase has a weak to moderate correlation with DOC, Cl^- and Fe_{tot}. The conductivity (σ') shows

411   a slightly stronger correlation with the DOC, the Cl^- and total iron concentration than the

412   polarization (σ''). The highest σ'' values (>100 μSm^{-1}) are related to the highest DOC and total

413   iron concentration.

414   Further evidence on the presence of the biogeochemical hot spot interpreted at the position of

415   S1 is available by the FTIR spectroscopy analysis of the freeze core samples presented in Fig.

416   11. The spectra show the absorbance intensity at different wavenumbers, C-O bond (~1050 cm$^-$

417   ^{1}), C=O double-bond (~1640 cm^{-1}), carboxyl (~1720 cm^{-1}), and O-H bonds (~3400 cm^{-1}). The

418   peaks are also indicated in Fig. 11 with the interpretation based on the typical values reported

419   in peatlands, for instance, McAnallen et al. (2018) or Artz et al. (2008).

420 **4 DISCUSSION**

421   4.1 Biogeochemical interpretation

422   The geochemical and geoelectrical parameters presented in Fig. 6-7 and 9 reveal consistent

423   patterns, with the highest values within the uppermost 10 cm around S1 and S3. The high DOC,

424   K^+ and phosphate concentrations in the uppermost peat layers and especially in the areas found

425   to be biogeochemically active, strongly suggest that there is rapid decomposition of dead plant

material in these areas (Bragazza et al., 2009). Ions such as K^+ and phosphate are essential plant nutrients, and phosphate species especially are often the primary limiting nutrient in peatlands (Hayati and Proctor, 1991). The presence of dissolved phosphate in pore waters suggests that (i) the plant uptake rate of this essential nutrient is exceeded by its production through the decomposition of plant material; and (ii) that organic matter turnover must be rapid indeed to deliver this amount of phosphate to the pore water. This is supported by the DOC concentrations in pore waters exceeding 10 mM. DOC is produced as a decomposition product during microbial hydrolysis and oxidation of solid phase organic carbon via enzymes such as phenol oxidase (Kang et al., 2018). Enzymatic oxidation processes are enhanced by oxygen ingress via diffusion and, more importantly, by water table fluctuations that work as an 'oxygen pump' to the shallow subsurface (Estop-Aragonés et al., 2012). Thus, an increased DOC concentration in the pore water can be used as an indicator for microbial activity (Elifantz et al., 2011; Liu, 2013). The small amount of phosphate measured in the less active area S2 can be explained by advective transport from the active area S1, which is direct 'up-stream' of S2. In this case, advective water flow through the uppermost peat layers along the hydrological head gradient may have transported a small amount of reaction products from the biogeochemical source areas to the 'non-active' area. The high DOC, Fe, K^+ and phosphate (only at S1) levels confirm our initial interpretation of the highly conductive and polarizable geophysical units within the first 20 - 50 cm bgs in the surroundings of S1 and S3 as biogeochemically active areas.

The high DOC concentrations are also likely to be directly or indirectly responsible for the Fe maximum in the upper layers. Dissolved Fe was predominantly found as Fe^{2+} (reducing conditions) suggesting either that high labile DOC levels maintain a low redox potential, or that the dissolved Fe^{2+} was complexed with the DOC limiting the oxidation kinetics enough so that Fe^{2+} can accumulate in peat pore waters. The TRIS analysis clearly showed very low levels of sulfide minerals in both freeze cores, especially in the uppermost peat layers. This was unexpected considering the reducing conditions implied by the dominance of pore water Fe^{2+}. We argue that the lack of sulfide minerals is due to insufficient H_2S or HS^- needed to form FeS or FeS_2, or that the redox potential was not low enough to reduce sulfate to H_2S or HS^-. Both mechanisms are possible, as groundwater in the catchment generally has low sulfate concentrations, and yet sulfate was detected in peat pore water samples, which would not be expected if redox potentials were low enough to reduce sulfate to sulfide. The chemical analyses do not reveal any significant or systemic vertical gradient in mineral sulfide concentrations, as expected for the site (Frei et al., 2012). The maximum in extractable (reactive) solid phase Fe was also located in the uppermost peat layer at the 'hot spot' S1. This Fe was likely in the form

460   of iron oxides or bound to/in the plant organic matter. Such iron rich layers typically form at

461   the redox boundary between oxic and anoxic zones and can be highly dynamic depending on

462   variations in the peatland water levels and oxygen ingress (Wang et al., 2017; Estop-Aragonés,

463   2013).

464   Similar to other peatlands (Artz et al., 2008), the FTIR spectra show the presence of carbon-

465   oxygen bonds such as C-O, C=O and COOH booth at S1 and S2. Furthermore, the peak

466   intensities at S1 tend to decrease with the depth, while the peak intensities at S2 samples tend

467   to increase in agreement with the increase in the polarization response (both phase and σ''). This

468   observation further supports our interpretation of the shallow 10 cm in IP images in the vicinity

469   of S1 as a biogeochemical hot spot. However, such biogeochemical hot spot is not related to

470   the accumulation of iron sulfides, which was suggested by Abdel Aal and Atekwana (2014) or

471   Wainwright et al. (2016) as the main parameter controlling the high IP response. The phosphate

472   and Fe could potentially form complexes with the O-H groups that show an absorbance peak at

473   1050 cm^{-1} (Arai and Sparks, 2001; Parikh and Chorover, 2006). Furthermore, the iron can also

474   form complexes with the carboxyl groups (absorbance at ~1720 cm^{-1}).

475   4.2 Correlation between the peat and the electrical signatures

476   The two electrical units observed within the peat indicate variations in the biogeochemical

477   activity with depth. Thus, it is likely that the anomalies associated with the highest σ', σ'', and

478   ϕ values in the uppermost unit correspond with the location of active biogeochemical zones,

479   i.e., a hot spot. Consequently, the moderate σ', σ'', and ϕ values indicate less biogeochemical

480   active or even inactive zone in the peat. The third unit represents the granitic bedrock. The low

481   metal content and the well-crystallized form of the granite lead to low σ'' values (here, < 40

482   μSm^{-1}), as suggested by Marshall and Madden (1959).

483   The high polarization response of the biogeochemically active peat (here $\sigma'' > 100$ μSm^{-1} and

484    $\phi > 18$ mrad) is consistent with the measurements of McAnallen et al. (2018), who performed

485   time-domain IP measurements in different peatlands. They suggest that the active peat is less

486   polarizable due to the presence of the abundant sphagnum cover. They found that in the areas

487   where the peat is actively accumulating, the ratio of the vascular plants and the non-vascular

488   sphagnum is low, and therefore, the oxygen availability is low. However, the sphagnum is

489   expected to exude a small amount of carbon into the peat, and Fenner et al. (2004) found that

490   the sphagnum contributes to the DOC leachate to the pore water, which is contradictory to the

491   model of McAnallen et al. (2018). In agreement with Fenner et al. (2004), in our study, we also

492   observe that high DOC content correlates with abundant sphagnum cover; which is also found

493   in conjunction with abundant purple moor-grass. In this regard, recent studies have

494   demonstrated an increase in the polarization response due to the accumulation of biomass and

495   activity in the root system (e.g., Weigand and Kemna 2017; Tsukanov and Schwartz, 2020).

496   However, the sphagnum does not have roots; thus, it cannot directly contribute to the

497   polarization response. McAnallen et al. (2018) suggest that the vascular purple moor-grass can

498   contribute to the high IP, as the roots transport oxygen into the deeper area, increasing the

499   wettability and normalized chargeability of the peat.

500   Derived from the results and discussion above, we delineated the geometry of the hot spots.

501   The map presented in Fig. 12 is based on the maps of phase and imaginary conductivity values

502   at a depth of 10 and 20 cm. Hot spots interpreted at those areas exceeding both a phase value

503   of 18 mrad and imaginary conductivity of 100 μSm^{-1} at the same time. Besides the geometry of

504   the hot spots, Fig. 12 indicates that the hot spot activity attenuates with the depth.

505   4.3 Possible polarization mechanisms

506   In this study, we have found a strong correlation between the polarization response (ϕ and σ'')

507   and Fe_{tot} in the solid phase and a less pronounced correlation between the polarization response

508   and the concentration of dissolved iron in the liquid phase (see Fig. 10). In all considered

509   mechanistic polarization models, the phase value depends on the volumetric content of metallic

510   particles (Wong, 1979; Revil 2015a, 2015b; Bücker et al., 2018, 2019; Feng et al, 2020) and

511   therefore, the phase could reveal the possible metallic content in the peat. If the iron in the solid

512   phase occurred in the form of highly conductive minerals, the two above correlations would

513   point to the polarization mechanism of perfect conductors described by Wong (1979) as a

514   possible explanation for the observed response. Previous studies (e.g., Flores Orozco et al.,

515   2011; 2013) attributed the polarization of iron sulfides (FeS or FeS_2) in sediments to such a

516   polarization mechanism as long as sufficient Fe^{2+} cations are available in the pore water. Such

517   effect has been investigated in detail by Bücker et al. (2018; 2019), regarding the changes in

518   the polarization response due to surface charge and reaction currents carried by redox reactions

519   of metal ions at the mineral surface. However, in the case of the present study, the lack of

520   sulfide, and the rather high pH (inferred from the presence of sulfate) in the pore water, do not

521   favor the precipitation of conductive sulfides such as pyrite. Under these conditions, iron would

522   rather precipitate as iron oxide or form iron-organic matter complexes. The electrical

523   conductivity of most iron oxides is orders of magnitude smaller than the conductivity of sulfides

524   (e.g., Cornell and Schwertmann, 1996), and is thus too low to explain an increased polarization

525   based on a perfect-conductor polarization model (e.g., Wong, 1979; Bücker et al., 2018, 2019;

Feng et al., 2020). The only highly conductive iron oxide is magnetite, with a conductivity similar to pyrite (Atekwana et al., 2016). Consequently, the presence of magnetite could explain such a polarization. However, the low pH (~5) typical for peat systems does not favor the precipitation of magnetite but rather less conducting iron (oxy)hydroxides such as ferrihydrite (Andrade et al., 2010; Linke and Gislason, 2018). Analysis of sediments of the freeze core did also not reveal magnetite. As indicated by the FTIR analysis, the iron might furthermore have built complexes with the carboxyl (absorbance at ~1720 cm^{-1}). Such moderately conductive iron minerals or iron-organic complexes might still cause a relatively strong polarization response as predicted by the polarization model developed by Revil et al. (2015) and Misra et al. (2016a). In this model, which attributes the polarization response to a diffuse intra-grain relaxation mechanism, the polarization magnitude is mainly controlled by the volumetric content. In this model, the (moderate) particle conductivity only plays a secondary role (e.g., Misra et al. 2016b).

The product of both surface charge density and specific surface area can be quantified by the Cation Exchange Capacity (CEC) of a material. As peat mainly consists of organic matter known to have a high CEC, even when compared to most clay minerals (e.g., Schwartz and Furman, 2014; and references therein), the polarization of charged organic surfaces may explain the observed IP response. Additionally, Garcia-Artigas et al. (2020) concluded that bioclogging due to fine particles and biofilms increases the specific surface area and the CEC, resulting in an increase in the polarization response. However, the CEC values measured in samples retrieved from the freeze core vary in a narrow range between 5 and 25 meq/kg and we did not observe any correlation between CEC and changes in the polarization magnitude (σ'', ϕ). Such lack of correlation between the polarization effect and the CEC was also reported by Ponziani et al. (2011), who conducted spectral IP measurements on a set of peat samples. Hence, the measured CEC is high enough to explain a rise in EDL-polarization; however, the (small) variation in CEC does not explain the observed variation in the polarization magnitude.

The pH of the pore fluid is also known to control the magnitude of EDL polarization; an increase of pH usually corresponds with an increase of the polarization magnitude (e.g., Skold et al., 2011). At low pH values, H^{+} ions occupy (negative) surface sites and thus reduce the net surface charge of the EDL (e.g., Hördt et al., 2016; and references therein). Our data seems to show the opposite behavior: we found a lower pH in the highly polarizable anomalies at S1 and S3 compared to site S2 (the inactive and less polarizable location); while the pH increases at depth for decreasing values in the polarization (both σ'' and ϕ). At the same time, variations in pH are

559 within the range 4.45 and 5.77 and thus might not be sufficiently large to control the observed

560 changes in the polarization response.

561 Besides pH, pore fluid salinity plays a significant role in the control of EDL polarization.

562 Laboratory measurements on sand and sandstone samples indicated that an increase in salinity

563 leads to an early rise of the imaginary conductivity, which is eventually followed by a peak and

564 a decrease at very high salinities during later stages of the experiments (e.g., Revil and Skold,

565 2011; Weller et al., 2015). Hördt et al. (2016) provided a possible theoretical explanation of

566 this behavior: In their membrane-polarization model, salinity controls the thickness of the

567 (diffuse layer) of the EDL and depending on the specific geometry of the pores; there is an

568 optimum thickness, which maximizes the magnitude of the polarization response. In the present

569 study, we observed that an increase in salinity (as indicated by the high Cl^- concentrations

570 within the uppermost 10 cm at all sampling locations) is associated with an increase in the

571 polarization magnitude response (e.g., Revil and Skold, 2011; Weller et al., 2015; Hördt et al.,

572 2016). However, the highest Cl^- concentrations were observed for the shallow layers at location

573 S2, where we measured lower polarization magnitudes (in terms of σ'', ϕ) compared to S1 and

574 S3.

575 The strong correlation between the polarization response and the DOC suggests an, as yet not

576 fully understood, causal relationship. A similar observation has recently been reported by Flores

577 Orozco et al. (2020), who found a strong correlation between the organic carbon content as a

578 proxy of microbial activity and both σ' and σ" in a municipal waste landfill in Austria.

579 Regarding the available carbon, McAnallen et al. (2018) reported a strong correlation between

580 the occurrence of long-chained C=O double bonds and the total chargeability of peat material.

581 The upper peat layers are exposed to oxygen leading to oxidation of the peat and formation of

582 C=O double bonds at solid phase surfaces and in the pore water DOC. Such long-chained

583 organic molecules have an increased wettability and thus more readily attach (or even form at

584 organic matter surfaces) to the surface of solid organic and mineral particles (Alonso et al.,

585 2009). Based on a membrane-polarization model, Bücker et al. (2017) predict an increase of

586 the polarization magnitude in the presence of wetting (i.e., long-chained) hydrocarbon in the

587 free phase. The long-chained polar DOC attaches to the peat surface, similar to polar

588 hydrocarbon, and so it might provide extra surface charge, thus reducing the pore space and

589 causing membrane polarization (Marshall and Madden, 1959).

590 As suggested by Vindedahl et al. (2016), organic matter can adsorb to the iron oxide surface

591 via electrostatic attraction and provides a negatively charged macromolecular layer on the iron

oxide. Such complexes could also explain the observed increase in the polarization response in the anomalies interpreted as biogeochemical hot spots. The point of zero charge of the peat is below pH 4 (Bakatula et al., 2018); while for iron (-oxide) is varying between ~5 and ~9 (Kosmulski et al., 2003). This means that the organic matter is probably negatively charged, and the iron oxide is most likely positively charged since the measured pH at the sample points is varying between 4.5 and 5.8 with lower values in the top 10 cm in the hot spot area. Hence, in the shallow 10 cm from S1 and S3, the pH favors the DOC to bond with the iron in the solid phase.

5 Conclusions

We investigated the applicability of induced polarization (IP) as a tool to identify and localize biogeochemically active areas or hot spots in peatlands. Although the exact polarization mechanism is not fully understood, our results reveal that the IP response of the peat changes with the level of biogeochemical activity. Thus, the IP method is capable of distinguishing between biogeochemical active and inactive zones within the peat. The phase and imaginary conductivity values show a contrast between these active and inactive zones and characterize the geometry of the hot spots even if iron sulfides are not present. The joint interpretation of chemical and geophysical data indicates that anomalous regions (characterized by phase values above 18 mrad and imaginary conductivity of 100 μSm^{-1}) delineate the geometry of the hot spots, which are limited to the top 10 cm bgs. Deeper areas (>10 cm) of the peat are less active. In this regard, our study shows that the induced polarization method is able to characterize biogeochemical changes and their geometry within peat with high resolution. Additionally, our study demonstrates the ability of the IP method to assess biogeochemically active zones even if they are not related to the microbiologically mediated accumulation of iron sulfides. We identify complexes of organic matter and iron as possible causes of the high polarization response of the carbon turnover hot spots investigated in our study. Further laboratory studies on peat samples with different concentrations and mixtures of DOC, phosphate, and iron in the pore fluid are required to fully understand the effect in IP signatures due to iron-organic complexes and the control phosphate exerts over the related polarization process.

625 Data availability

627 Competing interests.

628 The authors declare that they have no conflict of interest.

629 Author contribution

630 AFO and TK designed the experimental set-up, TK conducted the field survey and analysis of
631 the geophysical data. BG and SF conducted the geochemical measurements and their
632 interpretation. AFO, MB and TK interpreted the geophysical signatures. TK lead the
633 preparation of the draft, where SF, BG, MB and AFO contributed equally.
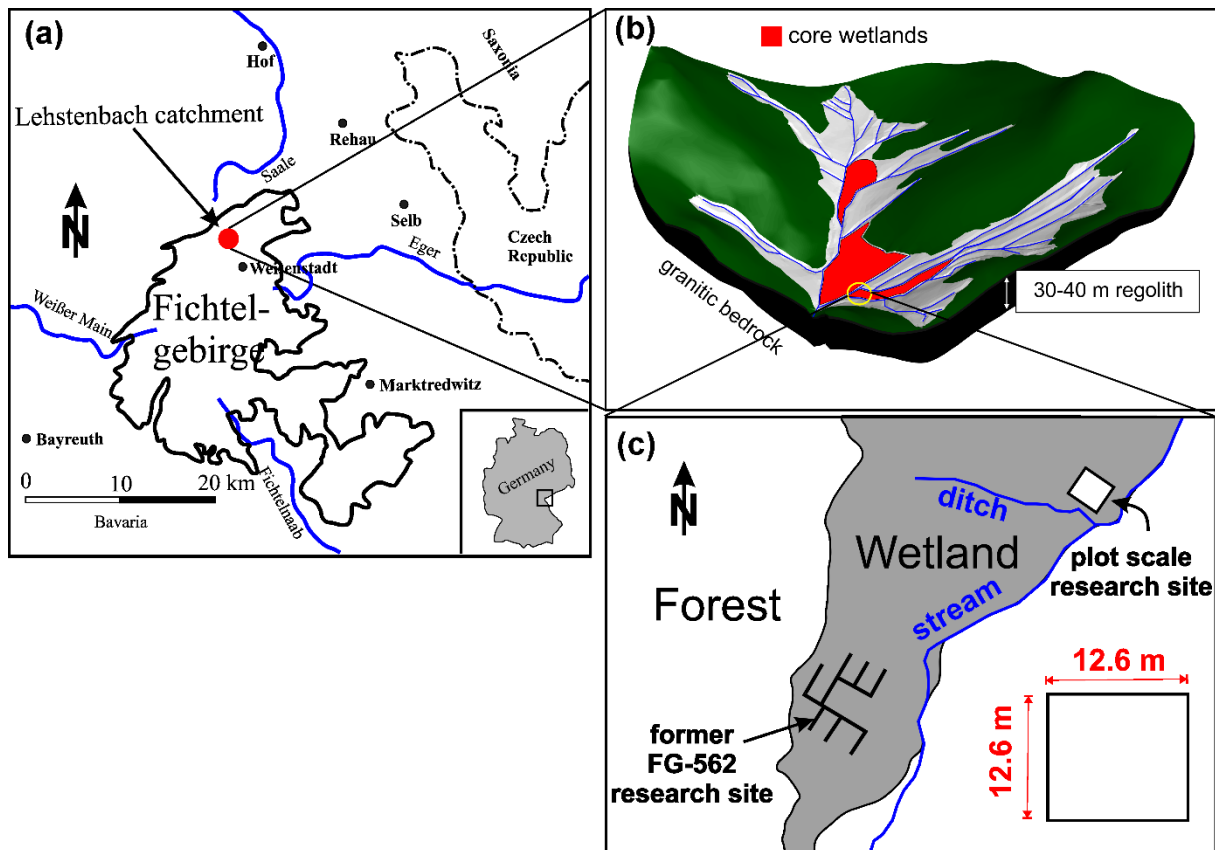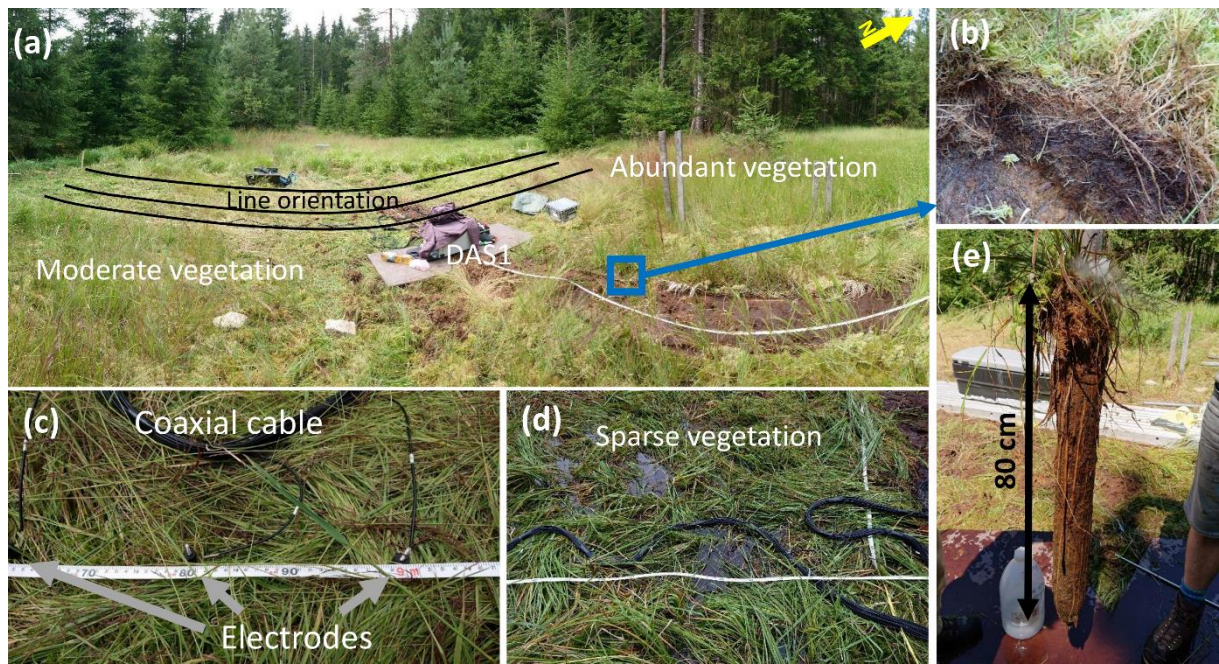
634

635

Figure 1: (a) General overview of the experimental plot located in the Fichtel Mountains and (b) structure of the bowl shaped Lehstenbach catchment, and (c) location of the experimental plot.

636

637

Figure 2: (a) Panoramic overview of the study site and the measurement setup. Pictures show the experimental setup and differences in the vegetation density between the northern and southern part of the experimental plot. The induced polarization (IP) lines appear distorted due to the panoramic view. (b) Sphagnum in the northern part of the experimental plot. (c) Coaxial cables and stainless steel electrodes used for IP measurements. (d) Vegetation and the coaxial cable bundle used for IP measurements at the water covered area in the southeastern part of the experimental plot. (e) The freeze core shows the internal structure of the peat.

638
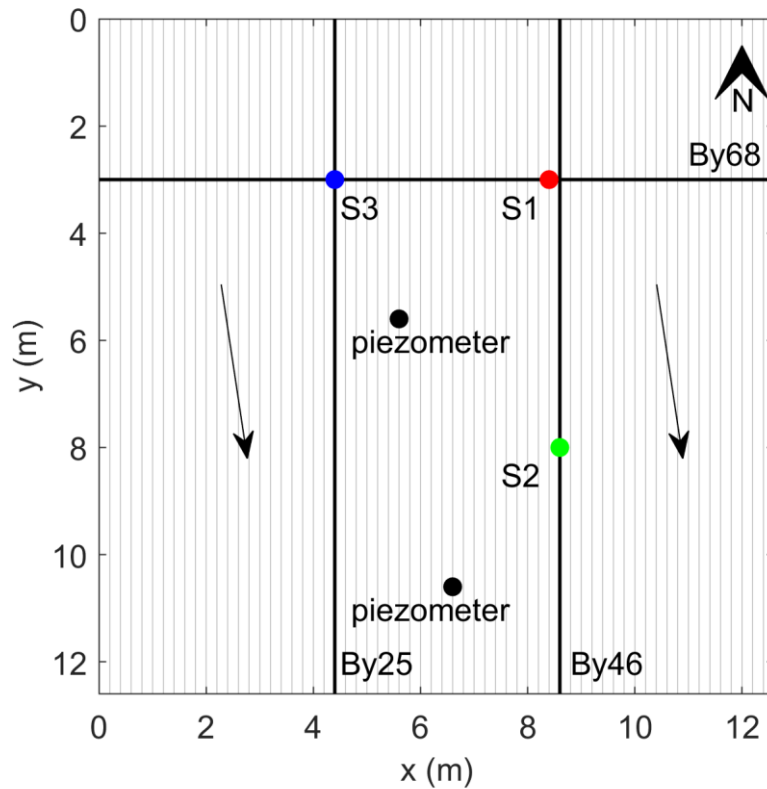
639

Figure 3: Schematic map of the experimental plot. The solid lines represent the measured profiles; the bold lines represent the position of the profiles discussed in this manuscript (By 25, By 46 and By 68). The arrows indicate the ground water flow direction. The points represent the locations of fluid (S1, S2 and S3) and freeze core (S1, S2) samples as well as the position of piezometric tubes, where the water level was measured.

640
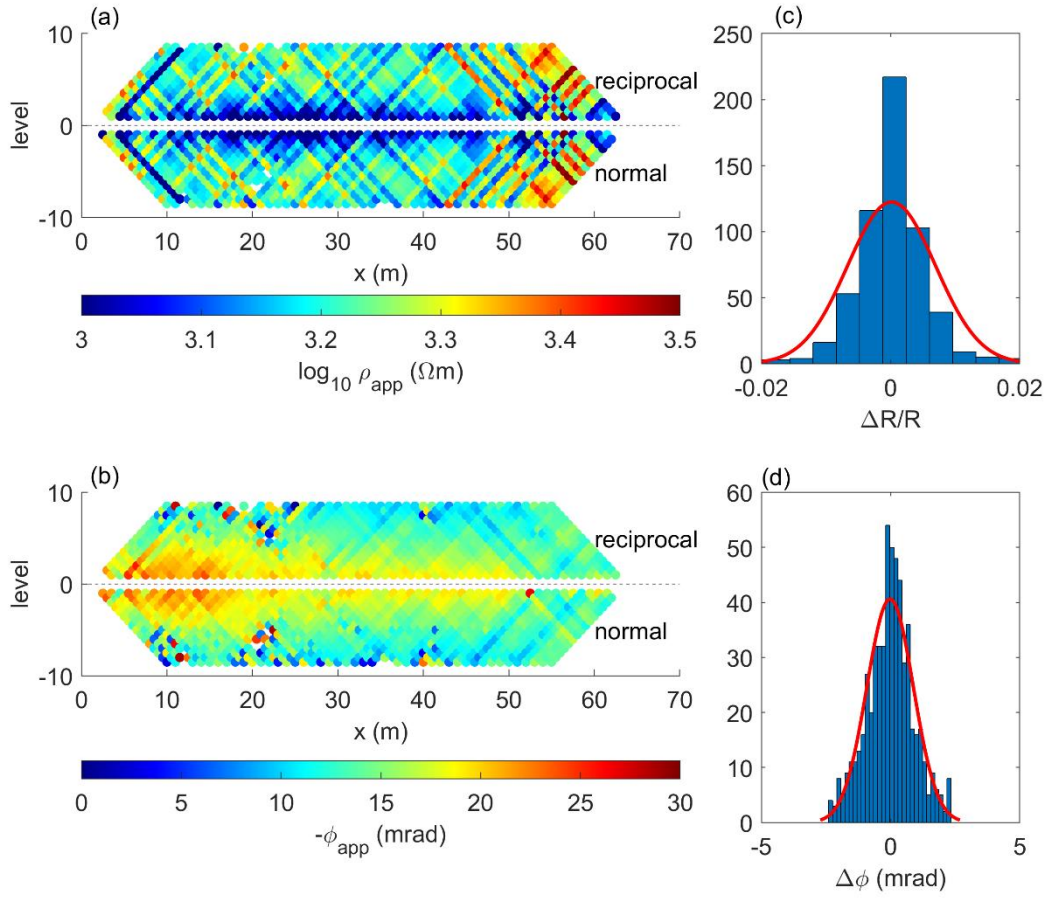
641

Figure 4: Raw data analysis. Raw-data pseudosections of (a) the apparent resistivity and (b) the apparent phase shift for measurements collected along profile By 25. Histograms of the normal-reciprocal misfits of (c) the measured resistance (normalized) and (d) the apparent phase shift.
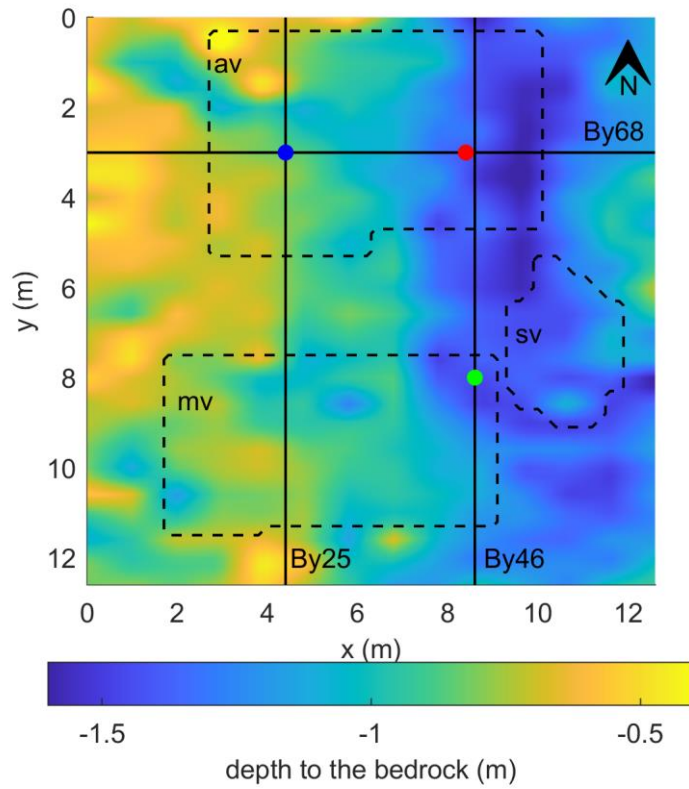
642

Figure 5: Variations in the thickness of the peat layer, i.e., depth to the granite bedrock. The positions of the three selected IP profiles By 25, By 46, and By 68 are indicated (solid lines) as well as the position of the sampling points and the geometry of the three classes of vegetation cover: abundant vegetation (av), moderate vegetation (mv), and sparse vegetation (sv).
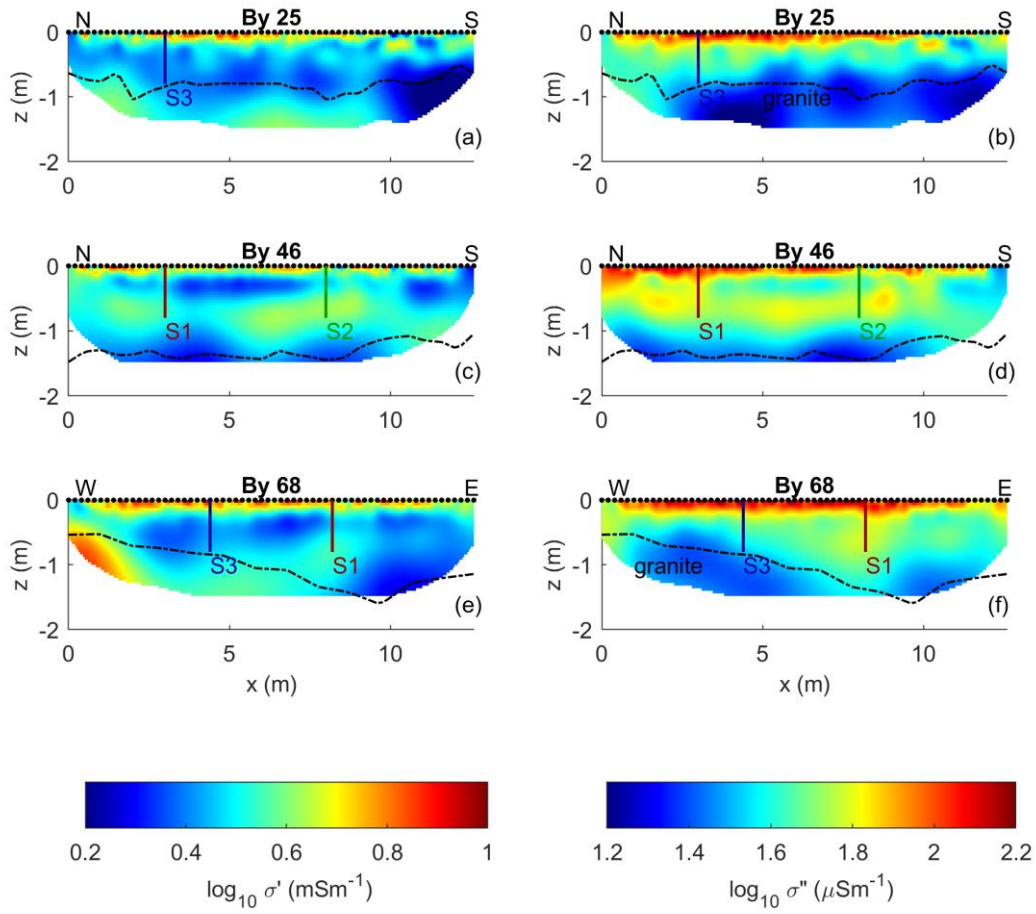
643

Figure 6: Imaging results for data collected along profiles By 25 (a-b), By 46 (c-d), and By 68 (e-f) expressed as real σ' and imaginary σ'' components of the complex conductivity. The dashed lines represent the contact between the peat and granite; the black dots show the electrode positions at the surface. The vertical lines represent the location of the fluid (S1, S2 and S3) and freeze core (S1, S2) samples.
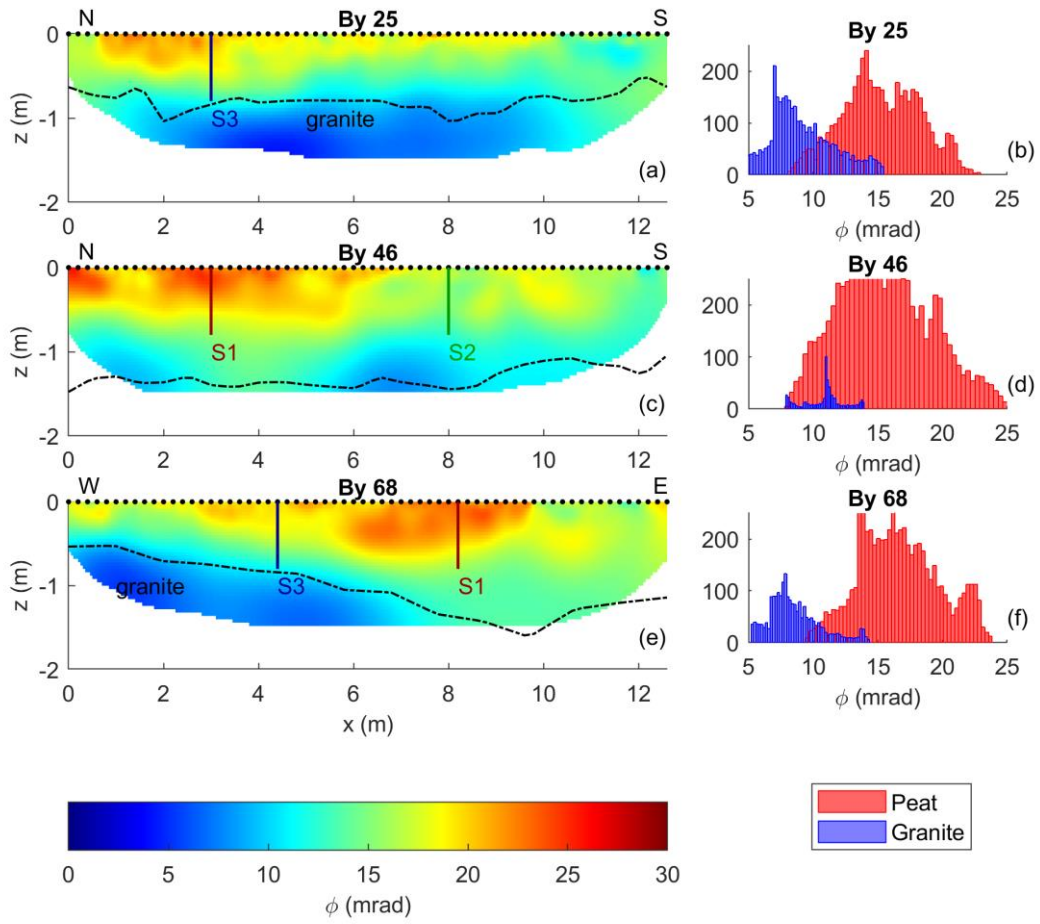
644

Figure 7: Imaging results for data collected along profiles By 25 (a), By 46 (c), and By 68 (e), expressed as phase values ϕ of the complex conductivity. The dashed lines represent the contact between peat and granite; the black dots show the electrode positions at the surface. The vertical lines represent the location of the fluid (S1, S2, S3) and freeze core (S1, S2) samples. The histograms represent the phase values of the granite and peat extracted from the imaging results in (6b, 6d, 6f) according to the geometry of the dashed lines.

645
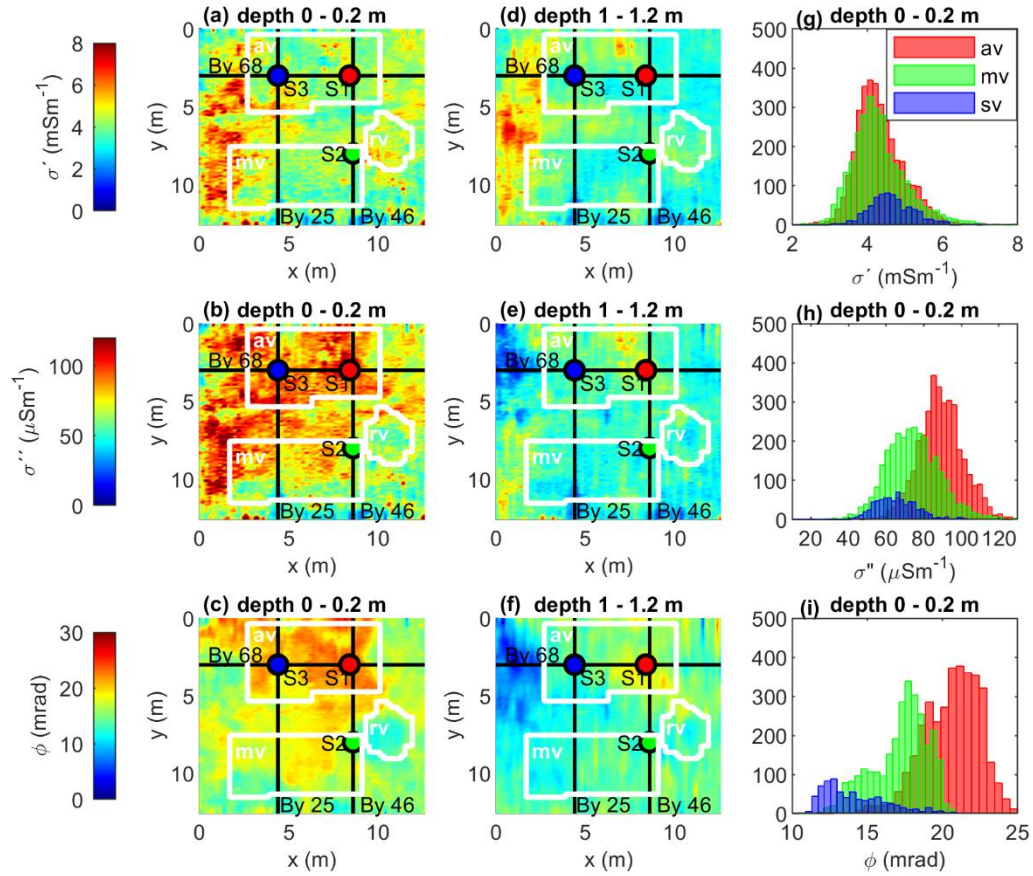
Figure 8: Maps of the complex conductivity at different depths. The black lines indicate the profiles By 25, By 46, and By 68. The dots represent the locations of the vertical sampling profiles S1, S2, and S3. The white lines outline areas classified as (av) abundant vegetation, (mv) moderate vegetation, (sv) sparse vegetation, and histograms of the complex-conductivity imaging results of the masked areas, the abundant vegetation (red bins), the moderate vegetation (green bins) and the sparse vegetation (blue bins).

646
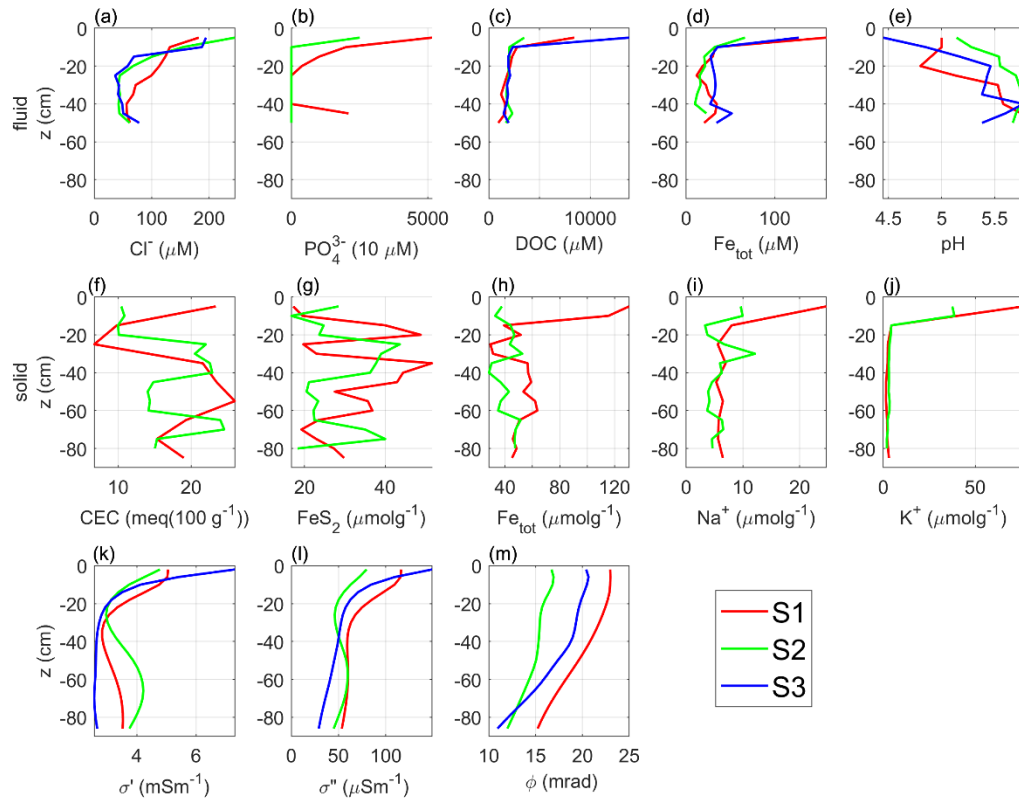
Figure 9: Results of geochemical analyses of water and soil samples. Fluid-sample analysis of the (a) chloride Cl$^-$, (b) phosphate PO$_4^{3-}$, (c) dissolved organic carbon, (d) total iron Fe$_{tot}$, and (e) pH. Freeze-core sample analysis of the (f) cation exchange capacity CEC, (g) iron sulfide FeS$_2$, (h) total iron Fe$_{tot}$, (i) sodium Na$^+$, and (j) potassium K$^+$. Imaging results at the three sampling locations in terms of (k) real component σ', (l) imaginary component σ'', and (m) phase φ of the complex conductivity.

647

648
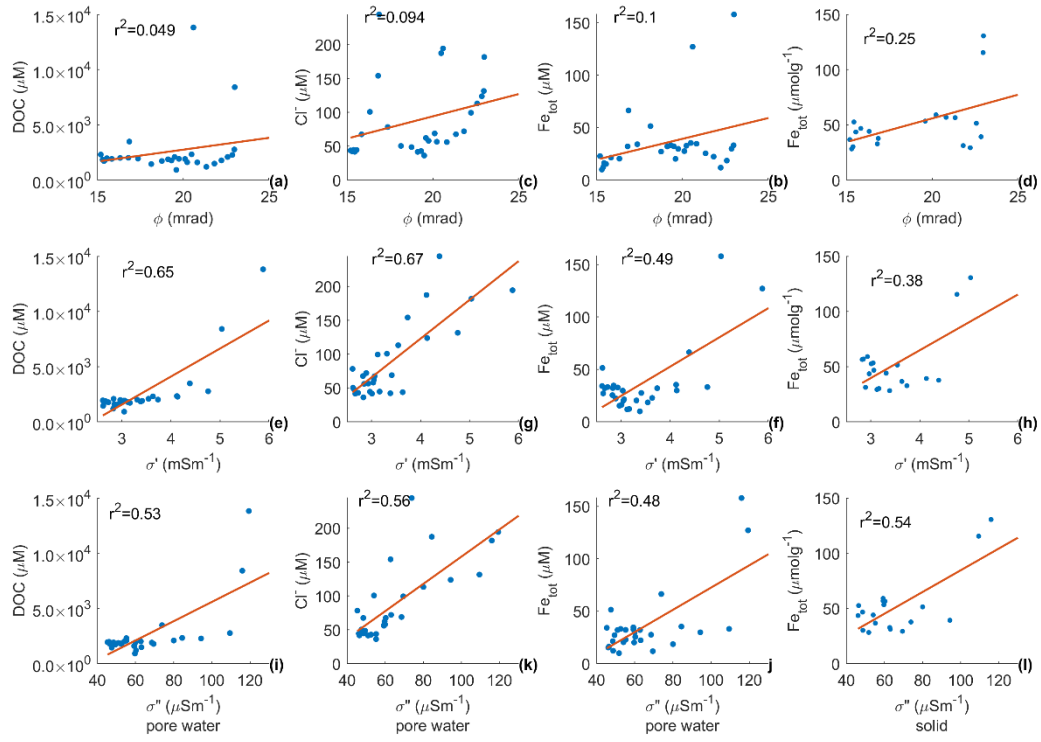
Figure 10: Correlations between the geophysical and geochemical parameters, phase (ϕ), the real (σ') and imaginary (σ'') component of the complex conductivity (retrieved from the imaging results) and the biogeochemical analysis, expressed in terms of the dissolved organic carbon (DOC), and chloride (Cl^-) content from the pore fluid samples and total iron (Fe_{tot}) content from pore fluid in $\mu moll^{-1}$ and solid samples in $\mu molg^{-1}$. The correlation coefficients of least square regressions analysis are shown in the top left corners of the subplots.

649
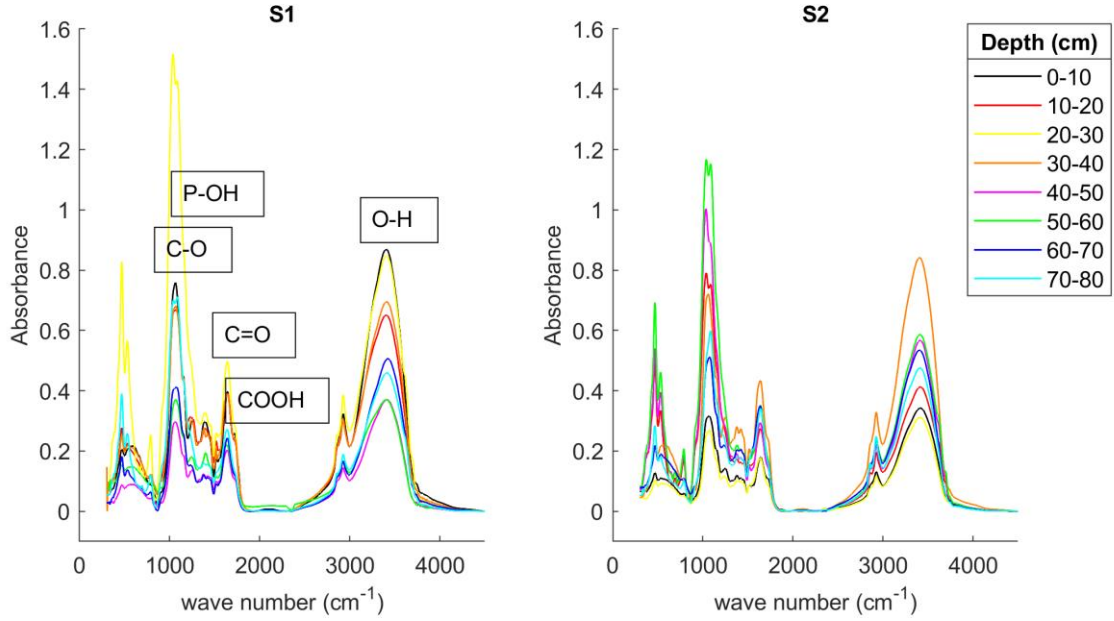
Figure 11: Fourier transform infrared (FTIR) spectroscopy of the freeze core samples collected at S1 (left panel) and S2 (right panel). Each sample was extracted from the 10 cm segments. The lines represent the depth at every 10 cm between 0 and 80 cm below ground surface. The relevant peaks show the absorbance intensity, the interpretation is based on Artz et al. (2008), Arai and Sparks (2001), Parikh and Chorover (2006).

Figure 12: Imaging results in terms of imaginary component of the complex conductivity $\sigma''>100\ \mu Sm^{-1}$, and phase $\phi>18$ mrad, indicating the hot spot geometry at depths of (a) 10 cm and at (b) 20 cm. The dots represent the locations of the vertical sampling profiles S1, S2, and S3.
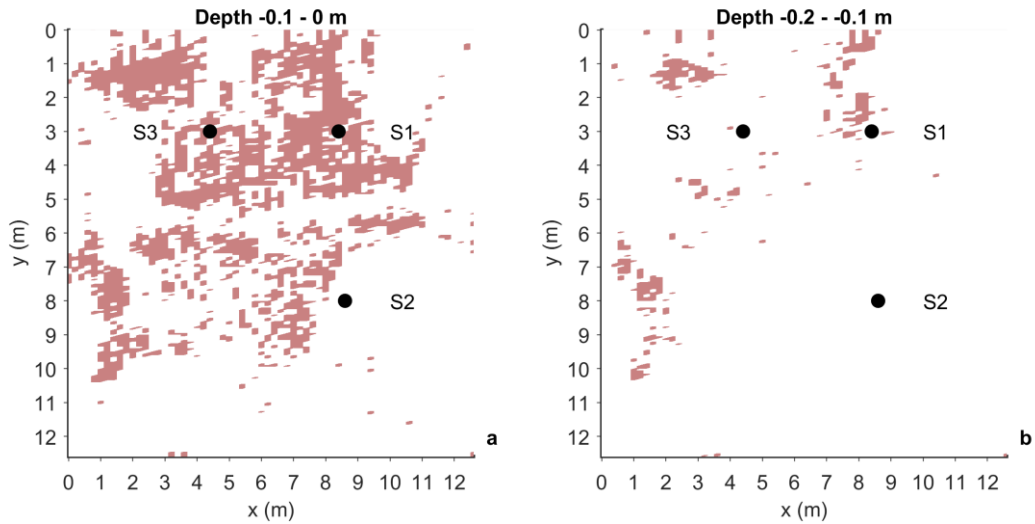
References

1. Abdel Aal, G. Z., & Atekwana, E. A. (2014). Spectral induced polarization (SIP) response of biodegraded oil in porous media. *Geophysical Journal International*, *196*(2), 804-817.

2. Abdel Aal, G. Z., Atekwana, E. A., Rossbach, S., & Werkema, D. D. (2010a). Sensitivity of geoelectrical measurements to the presence of bacteria in porous media. *Journal of Geophysical Research: Biogeosciences*, *115*(G3).

3. Abdel Aal, Gamal Z., Estella A. Atekwana, and Eliot A. Atekwana. "Effect of bioclogging in porous media on complex conductivity signatures." *Journal of Geophysical Research: Biogeosciences* 115, no. G3 (2010b).

4. Abdel Aal, G. Z., Atekwana, E. A., & Revil, A. (2014). Geophysical signatures of disseminated iron minerals: A proxy for understanding subsurface biophysicochemical processes. *Journal of Geophysical Research: Biogeosciences*, *119*(9), 1831-1849.

5. Albrecht, R., Gourry, J. C., Simonnot, M. O., & Leyval, C. (2011). Complex conductivity response to microbial growth and biofilm formation on phenanthrene spiked medium. *Journal of Applied Geophysics*, *75*(3), 558-564.

6. Alonso, D. M., Granados, M. L., Mariscal, R., & Douhal, A. (2009). Polarity of the acid chain of esters and transesterification activity of acid catalysts. *Journal of Catalysis*, *262*(1), 18-26.

7. Andrade, Â. L., Souza, D. M., Pereira, M. C., Fabris, J. D., & Domingues, R. Z. (2010). pH effect on the synthesis of magnetite nanoparticles by the chemical reduction-precipitation method. *Quimica Nova*, *33*(3), 524-527.

8. Arai, Y., & Sparks, D. L. (2001). ATR–FTIR spectroscopic investigation on phosphate adsorption mechanisms at the ferrihydrite–water interface. *Journal of Colloid and Interface Science*, *241*(2), 317-326.

685   9. Artz, R. R., Chapman, S. J., Robertson, A. J., Potts, J. M., Laggoun-Défarge, F., Gogo,
686   S., ... & Francez, A. J. (2008). FTIR spectroscopy can be used as a screening tool for
687   organic matter quality in regenerating cutover peatlands. *Soil Biology and*
688   *Biochemistry*, *40*(2), 515-527.

690   10. Atekwana, E., Patrauchan, M., & Revil, A. (2016). *Induced Polarization Signature of*
691   *Biofilms in Porous Media: From Laboratory Experiments to Theoretical Developments*
692   *and Validation* (No. DOE-Okstate-SC0007118). Oklahoma State Univ., Stillwater, OK
693   (United States).

695   11. Atekwana, E. A., & Slater, L. D. (2009). Biogeophysics: A new frontier in Earth science
696   research. *Reviews of Geophysics*, *47*(4).

698   12. Bakatula, E. N., Richard, D., Neculita, C. M., & Zagury, G. J. (2018). Determination of
699   point of zero charge of natural organic materials. *Environmental Science and Pollution*
700   *Research*, *25*(8), 7823-7833.

702   13. Biester, H., Knorr, K. H., Schellekens, J., Basler, A., & Hermanns, Y. M. (2014).
703   Comparison of different methods to determine the degree of peat decomposition in
704   peat bogs. *Biogeosciences*, *11*(10), 2691-2707.

706   14. Binley, A., & Kemna, A. (2005). DC resistivity and induced polarization methods. In
707   *Hydrogeophysics* (pp. 129-156). Springer, Dordrecht.

709   15. Binley, A., & Slater, L. (2020). *Resistivity and Induced Polarization: Theory and*
710   *Applications to the Near-surface Earth*. Cambridge University Press.

713   16. Binley, A., Hubbard, S. S., Huisman, J. A., Revil, A., Robinson, D. A., Singha, K., &
714   Slater, L. D. (2015). The emergence of hydrogeophysics for improved understanding of
715   subsurface processes over multiple scales. *Water resources research*, *51*(6), 3837-3866.
716

17. Boano, F., Harvey, J. W., Marion, A., Packman, A. I., Revelli, R., Ridolfi, L., & Wörman, A. (2014). Hyporheic flow and transport processes: Mechanisms, models, and biogeochemical implications. *Reviews of Geophysics*, *52*(4), 603-679.

18. Bragazza, L., Buttler, A., Siegenthaler, A., & Mitchell, E. A. (2009). Plant litter decomposition and nutrient release in peatlands. *Geoph. Monog. Series*, *184*, 99-110.

19. Bücker, M., & Hördt, A. (2013). Analytical modelling of membrane polarization with explicit parametrization of pore radii and the electrical double layer. *Geophysical Journal International*, *194*(2), 804-813.

20. Bücker, M., Orozco, A. F., Hördt, A., & Kemna, A. (2017). An analytical membrane-polarization model to predict the complex conductivity signature of immiscible liquid hydrocarbon contaminants. *Near Surface Geophysics*, *15*(6), 547-562.

21. Bücker, M., Orozco, A. F., & Kemna, A. (2018). Electrochemical polarization around metallic particles—Part 1: The role of diffuse-layer and volume-diffusion relaxation. *Geophysics*, *83*(4), E203-E217.

22. Bücker, M., Undorf, S., Flores Orozco, A., & Kemna, A. (2019). Electrochemical polarization around metallic particles—Part 2: The role of diffuse surface charge. *Geophysics*, *84*(2), E57-E73.

23. Canfield, D. E. (1989). Reactive iron in marine sediments. *Geochimica et Cosmochimica Acta*, *53*(3), 619-632.

24. Canfield, D. E., Raiswell, R., Westrich, J. T., Reaves, C. M., & Berner, R. A. (1986). The use of chromium reduction in the analysis of reduced inorganic sulfur in sediments and shales. *Chemical geology*, *54*(1-2), 149-155.

25. Capps, K. A., & Flecker, A. S. (2013). Invasive fishes generate biogeochemical hotspots in a nutrient-limited system. *PLoS One*, *8*(1), e54093.

26. Cirmo, C. P., & McDonnell, J. J. (1997). Linking the hydrologic and biogeochemical controls of nitrogen transport in near-stream zones of temperate-forested catchments: a review. *Journal of Hydrology*, *199*(1-2), 88-120.

27. Cornell, R. M., & Schwertmann, U. (1996). The Iron Oxides, VCH.

28. Costanza, R., d'Arge, R., De Groot, R., Farber, S., Grasso, M., Hannon, B., ... & Raskin, R. G. (1997). The value of the world's ecosystem services and natural capital. *nature*, *387*(6630), 253-260.

29. Costanza, R., De Groot, R., Braat, L., Kubiszewski, I., Fioramonti, L., Sutton, P., ... & Grasso, M. (2017). Twenty years of ecosystem services: how far have we come and how far do we still need to go?. *Ecosystem services*, *28*, 1-16.

30. Davis, C. A., Atekwana, E., Atekwana, E., Slater, L. D., Rossbach, S., & Mormile, M. R. (2006). Microbial growth and biofilm formation in geologic media is detected with complex conductivity measurements. *Geophysical Research Letters*, *33*(18).

31. Diamond, J. S., McLaughlin, D. L., Slesak, R. A., & Stovall, A. (2020). Microtopography is a fundamental organizing structure of vegetation and soil chemistry in black ash wetlands.

32. Durejka, S., Gilfedder, B. S., & Frei, S. (2019). A method for long-term high resolution 222Radon measurements using a new hydrophobic capillary membrane system. *Journal of environmental radioactivity*, *208*, 105980.

33. Elifantz, H., Kautsky, L., Mor-Yosef, M., Tarchitzky, J., Bar-Tal, A., Chen, Y., & Minz, D. (2011). Microbial activity and organic matter dynamics during 4 years of irrigation with treated wastewater. *Microbial ecology*, *62*(4), 973-981.

34. Estop-Aragonés, C., Knorr, K. H., & Blodau, C. (2012). Controls on in situ oxygen and dissolved inorganic carbon dynamics in peats of a temperate fen. *Journal of Geophysical Research: Biogeosciences*, *117*(G2).

784 35. Estop-Aragonés, C., Knorr, K. H., & Blodau, C. (2013). Belowground in situ redox
785 dynamics and methanogenesis recovery in a degraded fen during dry-wet cycles and
786 flooding. *Biogeosciences*, *10*(1), 421-436.
787
788 36. Feng, L., Li, Q., Cameron, S. D., He, K., Colby, R., Walker, K. M., ... & Ertaş, D.
789 (2020). Quantifying induced polarization of conductive inclusions in porous Media
790 and implications for Geophysical Measurements. *Scientific reports*, *10*(1), 1-12.
791

792 37. Fenner, N., Ostle, N., Freeman, C., Sleep, D., & Reynolds, B. (2004). Peatland carbon
793 efflux partitioning reveals that Sphagnum photosynthate contributes to the DOC pool.
794 *Plant and Soil*, *259*(1-2), 345-354.
795

796 38. Flores Orozco, A., Williams, K.H., Long, P.E., Hubbard, S.S. and Kemna, A., 2011.
797 Using complex resistivity imaging to infer biogeochemical processes associated with
798 bioremediation of an uranium-contaminated aquifer. *Journal of Geophysical Research:*
799 *Biogeosciences*, *116*(G3).
800

801 39. Flores Orozco, A., Kemna, A., & Zimmermann, E. (2012a). Data error quantification in
802 spectral induced polarization imaging. *Geophysics*, *77*(3), E227-E237.
803

804 40. Flores Orozco, A., Kemna, A., Oberdörster, C., Zschornack, L., Leven, C., Dietrich, P.,
805 & Weiss, H. (2012b). Delineation of subsurface hydrocarbon contamination at a former
806 hydrogenation plant using spectral induced polarization imaging. *Journal of*
807 *contaminant hydrology*, *136*, 131-144.
808

809 41. Flores Orozco, A., Williams, K. H., & Kemna, A. (2013). Time-lapse spectral induced
810 polarization imaging of stimulated uranium bioremediation. *Near Surface Geophysics*,
811 *11*(5), 531-544.
812

813 42. Flores Orozco, A., Velimirovic, M., Tosco, T., Kemna, A., Sapion, H., Klaas, N., ... &
814 Bastiaens, L. (2015). Monitoring the injection of microscale zerovalent iron particles
815 for groundwater remediation by means of complex electrical conductivity imaging.
816 *Environmental Science & Technology*, *49*(9), 5593-5600.

43. Flores Orozco, A., Kemna, A., Binley, A., & Cassiani, G. (2019). Analysis of time-lapse data error in complex conductivity imaging to alleviate anthropogenic noise for site characterization. *Geophysics*, *84*(2), B181-B193.

44. Flores Orozco, A., Gallistl, J., Steiner, M., Brandstätter, C., & Fellner, J. (2020). Mapping biogeochemically active zones in landfills with induced polarization imaging: The Heferlbach landfill. *Waste Management*, *107*, 121-132.

45. Flores Orozco, A., Aigner, L. and Gallistl, J., 2021. Investigation of cable effects in spectral induced polarization imaging at the field scale using multicore and coaxial cables. *Geophysics*, *86*(1), pp.E59-E75.

46. Frei, S., Lischeid, G., & Fleckenstein, J. H. (2010). Effects of micro-topography on surface–subsurface exchange and runoff generation in a virtual riparian wetland—A modeling study. *Advances in Water Resources*, *33*(11), 1388-1401.

47. Frei, S., Knorr, K. H., Peiffer, S., & Fleckenstein, J. H. (2012). Surface micro-topography causes hot spots of biogeochemical activity in wetland systems: A virtual modeling experiment. *Journal of Geophysical Research: Biogeosciences*, *117*(G4).

48. Garcia-Artigas, R., Himi, M., Revil, A., Urruela, A., Lovera, R., Sendrós, A., ... & Rivero, L. (2020). Time-domain induced polarization as a tool to image clogging in treatment wetlands. *Science of The Total Environment*, *724*, 138189.

49. deGroot-Hedlin, C., & Constable, S. (1990). Occam's inversion to generate smooth, two-dimensional models from magnetotelluric data. *Geophysics*, *55*(12), 1613-1624.

50. Gu, B., Liang, L., Dickey, M. J., Yin, X., & Dai, S. (1998). Reductive precipitation of uranium (VI) by zero-valent iron. *Environmental Science & Technology*, *32*(21), 3366-3373.

850   51. Gutknecht, J. L., Goodman, R. M., & Balser, T. C. (2006). Linking soil process and
851   microbial ecology in freshwater wetland ecosystems. *Plant and Soil*, *289*(1-2), 17-34.
852

853   52. Hansen, D. J., McGuire, J. T., Mohanty, B. P., & Ziegler, B. A. (2014). Evidence of
854   aqueous iron sulfid clusters in the vadose zone. *Vadose Zone Journal*, *13*(3), 1-12.
855

856   53. Hartley, A. E., & Schlesinger, W. H. (2000). Environmental controls on nitric oxide
857   emission from northern Chihuahuan desert soils. *Biogeochemistry*, *50*(3), 279-300.
858

859   54. Hayati, A. A., & Proctor, M. C. F. (1991). Limiting nutrients in acid-mire vegetation:
860   peat and plant analyses and experiments on plant responses to added nutrients. *The*
861   *Journal of Ecology*, 75-95.
862

863   55. Hördt, A., Bairlein, K., Bielefeld, A., Bücker, M., Kuhn, E., Nordsiek, S. and Stebner,
864   H., 2016. The dependence of induced polarization on fluid salinity and pH, studied with
865   an extended model of membrane polarization. *Journal of Applied Geophysics*, *135*,
866   pp.408-417.
867

868   56. Kang, H., Kwon, M. J., Kim, S., Lee, S., Jones, T. G., Johncock, A. C., ... & Freeman,
869   C. (2018). Biologically driven DOC release from peatlands during recovery from
870   acidification. *Nature communications*, *9*(1), 1-7.
871

872   57. Kayranli, B., Scholz, M., Mustafa, A., & Hedmark, Å. (2010). Carbon storage and
873   fluxes within freshwater wetlands: a critical review. *Wetlands*, *30*(1), 111-124.
874

875   58. Kemna, A., 2000. Tomographic Inversion of Complex Resistivity: Theory and
876   Application.Der Andere Verlag Osnabrück, Germany
877

878

879   59. Kemna, A., Binley, A., Ramirez, A., & Daily, W. (2000). Complex resistivity
880   tomography for environmental applications. *Chemical Engineering Journal*, *77*(1-2),
881   11-18.
882

883 60. Kemna, A., Vanderborght, J., Kulessa, B., & Vereecken, H. (2002). Imaging and
884   characterisation of subsurface solute transport using electrical resistivity tomography
885   (ERT) and equivalent transport models. *Journal of Hydrology*, *267*(3-4), 125-146.
886

887 61. Kemna, A., Binley, A., & Slater, L. (2004). Crosshole IP imaging for engineering and
888   environmental applications. *Geophysics*, *69*(1), 97-107.
889

890 62. Kemna, A., Binley, A., Cassiani, G., Niederleithinger, E., Revil, A., Slater, L., ... &
891   Kruschwitz, S. (2012). An overview of the spectral induced polarization method for
892   near-surface applications. *Near Surface Geophysics*, *10*(6), 453-468.
893

894 63. Kessouri, P., Furman, A., Huisman, J. A., Martin, T., Mellage, A., Ntarlagiannis, D., ...
895   & Kemna, A. (2019). Induced polarization applied to biogeophysics: recent advances
896   and future prospects. *Near Surface Geophysics*, *17*(6-Recent Developments in Induced
897   Polarization), 595-621.
898

899 64. Kleinebecker, T., Hölzel, N., & Vogel, A. (2008). South Patagonian ombrotrophic bog
900   vegetation reflects biogeochemical gradients at the landscape level. *Journal of
901   vegetation science*, *19*(2), 151-160.
902

903 65. Kosmulski, M., Maczka, E., Jartych, E., & Rosenholm, J. B. (2003). Synthesis and
904   characterization of goethite and goethite–hematite composite: experimental study and
905   literature survey. *Advances in colloid and interface science*, *103*(1), 57-76.
906

907 66. LaBrecque, D. J., Miletto, M., Daily, W., Ramirez, A., & Owen, E. (1996). The effects
908   of noise on Occam's inversion of resistivity tomography data. *Geophysics*, *61*(2), 538-
909   548.
910

911 67. Leroy, P., Revil, A., Kemna, A., Cosenza, P., & Ghorbani, A. (2008). Complex
912   conductivity of water-saturated packs of glass beads. *Journal of colloid and interface
913   science*, *321*(1), 103-117.
914

915   68. Lesmes, D. P., & Frye, K. M. (2001). Influence of pore fluid chemistry on the
916   complex conductivity and induced polarization responses of Berea sandstone. *Journal*
917   *of Geophysical Research: Solid Earth*, *106*(B3), 4079-4090.

918

919   69. Linke, T., & Gislason, S. R. (2018). Stability of iron minerals in Icelandic peat areas
920   and transport of heavy metals and nutrients across oxidation and salinity gradients–a
921   modelling approach. *Energy Procedia*, *146*, 30-37.

922

923   70. Lischeid, G., Kolb, A., & Alewell, C. (2002). Apparent translatory flow in
924   groundwater recharge and runoff generation. *Journal of Hydrology*, *265*(1-4), 195-
925   211.

926

927   71. Liu, H. (2013). Thermal response of soil microbial respiration is positively associated
928   with labile carbon content and soil microbial activity. *Geoderma*, *193*, 275-281.

929

930   72. Mansoor, N., & Slater, L. (2007). On the relationship between iron concentration and
931   induced polarization in marsh soils. *Geophysics*, *72*(1), A1-A5.

932

933   73. Marshall, D. J., & Madden, T. R. (1959). Induced polarization, a study of its causes.
934   *Geophysics*, *24*(4), 790-816.

935

936   74. Maurya, P. K., Rønde, V. K., Fiandaca, G., Balbarini, N., Auken, E., Bjerg, P. L., &
937   Christiansen, A. V. (2017). Detailed landfill leachate plume mapping using 2D and 3D
938   electrical resistivity tomography-with correlation to ionic strength measured in screens.
939   *Journal of Applied Geophysics*, *138*, 1-8.

940

941   75. McAnallen, L., Doherty, R., Donohue, S., Kirmizakis, P., & Mendonça, C. (2018).
942   Combined use of geophysical and geochemical methods to assess areas of active,
943   degrading and restored blanket bog. *Science of the Total Environment*, *621*, 762-771.

944

945   76. McClain, M. E., Boyer, E. W., Dent, C. L., Gergel, S. E., Grimm, N. B., Groffman, P.
946   M., ... & McDowell, W. H. (2003). Biogeochemical hot spots and hot moments at the
947   interface of terrestrial and aquatic ecosystems. *Ecosystems*, 301-312.

948

949 77. Mellage, A., Smeaton, C. M., Furman, A., Atekwana, E. A., Rezanezhad, F., & Van
950 Cappellen, P. (2018). Linking spectral induced polarization (SIP) and subsurface
951 microbial processes: Results from sand column incubation experiments. *Environmental*
952 *science & technology*, *52*(4), 2081-2090.

953

954 78. Mishra, U., & Riley, W. J. (2015). Scaling impacts on environmental controls and
955 spatial heterogeneity of soil organic carbon stocks. *Biogeosciences Discussions*
956 *(Online)*, *12*(2).

957

958 79. Misra, S., Torres-Verdín, C., Revil, A., Rasmus, J., & Homan, D. (2016a). Interfacial
959 polarization of disseminated conductive minerals in absence of redox-active species—
960 Part 1: Mechanistic model and validation. *Geophysics*, *81*(2), E139-E157.

961

962 80. Misra, S., Torres-Verdín, C., Revil, A., Rasmus, J., & Homan, D. (2016b). Interfacial
963 polarization of disseminated conductive minerals in absence of redox-active species—
964 Part 2: Effective electrical conductivity and dielectric permittivity Interfacial
965 polarization due to inclusions. *Geophysics*, *81*(2), E159-E176.

966

967 81. Morse, J. L., Werner, S. F., Gillin, C. P., Goodale, C. L., Bailey, S. W., McGuire, K. J.,
968 & Groffman, P. M. (2014). Searching for biogeochemical hot spots in three dimensions:
969 Soil C and N cycling in hydropedologic settings in a northern hardwood forest. *Journal*
970 *of Geophysical Research: Biogeosciences*, *119*(8), 1596-1607.

971

972 82. Ntarlagiannis, D., Williams, K. H., Slater, L., & Hubbard, S. (2005). Low-frequency
973 electrical response to microbial induced sulfid precipitation. *Journal of Geophysical*
974 *Research: Biogeosciences*, *110*(G2).

975

976 83. Ntarlagiannis, D., Doherty, R. and Williams, K.H., 2010. Spectral induced polarization
977 signatures of abiotic FeS precipitation SIP signatures of FeS precipitation. *Geophysics*,
978 *75*(4), pp.F127-F133.

979

980 84. Parikh, S. J., & Chorover, J. (2006). ATR-FTIR spectroscopy reveals bond formation
981 during bacterial adhesion to iron oxide. *Langmuir*, *22*(20), 8492-8500.

982

983   85. Parry, L. E., West, L. J., Holden, J., & Chapman, P. J. (2014). Evaluating approaches

984   for estimating peat depth. *Journal of Geophysical Research: Biogeosciences*, *119*(4),

985   567-576.

986

987   86. Partington, D., Brunner, P., Frei, S., Simmons, C. T., Werner, A. D., Therrien, R., ... &

988   Fleckenstein, J. H. (2013). Interpreting streamflow generation mechanisms from

989   integrated surface-subsurface flow models of a riparian wetland and catchment. *Water*

990   *Resources Research*, *49*(9), 5501-5519.

991

992   87. Pelton, W. H., Ward, S. H., Hallof, P. G., Sill, W. R., & Nelson, P. H. (1978). Mineral

993   discrimination and removal of inductive coupling with multifrequency IP. *Geophysics*,

994   *43*(3), 588-609.

995

996   88. Personna, Y. R., Ntarlagiannis, D., Slater, L., Yee, N., O'Brien, M., & Hubbard, S.

997   (2008). Spectral induced polarization and electrodic potential monitoring of microbially

998   mediated iron sulfid transformations. *Journal of Geophysical Research: Biogeosciences*,

999   *113*(G2).

1000

1001   89. Placencia-Gómez, E., Slater, L., Ntarlagiannis, D., & Binley, A. (2013). Laboratory SIP

1002   signatures associated with oxidation of disseminated metal sulfids. *Journal of*

1003   *Contaminant Hydrology*, *148*, 25-38.

1004

1005   90. Ponziani, M., Slob, E. C., Ngan-Tillard, D. J. M., & Vanhala, H. (2011). Influence of

1006   water content on the electrical conductivity of peat. *International Water Technology*

1007   *Journal*, *1*(1), 14-21.

1008

1009   91. Qi, Y., Soueid Ahmed, A., Revil, A., Ghorbani, A., Abdulsamad, F., Florsch, N., &

1010   Bonnenfant, J. (2018). Induced polarization response of porous media with metallic

1011   particles—Part 7: Detection and quantification of buried slag heaps. *Geophysics*,

1012   *83*(5), E277-E291.

1013

1014   92. Revil, A. (2012). Spectral induced polarization of shaly sands: Influence of the electrical

1015   double layer. *Water Resources Research*, *48*(2).

1016

93. Revil, A., & Florsch, N. (2010). Determination of permeability from spectral induced polarization in granular media. *Geophysical Journal International*, *181*(3), 1480-1498.

94. Revil, A., & Skold, M. (2011). Salinity dependence of spectral induced polarization in sands and sandstones. *Geophysical Journal International*, *187*(2), 813-824.

95. Revil, A., Atekwana, E., Zhang, C., Jardani, A., & Smith, S. (2012). A new model for the spectral induced polarization signature of bacterial growth in porous media. *Water Resources Research*, *48*(9).

96. Revil, A., Florsch, N., & Mao, D. (2015a). Induced polarization response of porous media with metallic particles—Part 1: A theory for disseminated semiconductors. *Geophysics*, *80*(5), D525-D538.

97. Revil, A., Abdel Aal, G. Z., Atekwana, E. A., Mao, D., & Florsch, N. (2015b). Induced polarization response of porous media with metallic particles—Part 2: Comparison with a broad database of experimental data. *Geophysics*, *80*(5), D539-D552.

98. Revil, A., Coperey, A., Shao, Z., Florsch, N., Fabricius, I. L., Deng, Y., ... & van Baaren, E. S. (2017a). Complex conductivity of soils. *Water Resources Research*, *53*(8), 7121-7147.

99. Revil, A., Sleevi, M. F., & Mao, D. (2017b). Induced polarization response of porous media with metallic particles—Part 5: Influence of the background polarization. *Geophysics*, *82*(2), E77-E96.

100. Revil, A., Mao, D., Shao, Z., Sleevi, M. F., & Wang, D. (2017c). Induced polarization response of porous media with metallic particles—Part 6: The case of metals and semimetals. *Geophysics*, *82*(2), E97-E110.

101. Revil, A., Coperey, A., Mao, D., Abdulsamad, F., Ghorbani, A., Rossi, M., & Gasquet, D. (2018). Induced polarization response of porous media with metallic particles—Part 8: Influence of temperature and salinity. *Geophysics*, *83*(6), E435-E456.

102. Rosier, C. L., Atekwana, E. A., Aal, G. A., & Patrauchan, M. A. (2019). Cell concentrations and metabolites enhance the SIP response to biofilm matrix components. *Journal of Applied Geophysics*, *160*, 183-194.

103. Schurr, J. M. (1964). On the theory of the dielectric dispersion of spherical colloidal particles in electrolyte solution1. *The Journal of Physical Chemistry*, *68*(9), 2407-2413.

104. Schwartz, N., & Furman, A. (2014). On the spectral induced polarization signature of soil organic matter. *Geophysical Journal International*, *200*(1), 589-595.

105. Schwarz, G. (1962). A theory of the low-frequency dielectric dispersion of colloidal particles in electrolyte solution1, 2. *The Journal of Physical Chemistry*, *66*(12), 2636-2642.

106. Seigel, H., Nabighian, M., Parasnis, D. S., & Vozoff, K. (2007). The early history of the induced polarization method. *The Leading Edge*, *26*(3), 312-321.

107. Skold, M., Revil, A., & Vaudelet, P. (2011). The pH dependence of spectral induced polarization of silica sands: Experiment and modeling. *Geophysical Research Letters*, *38*(12).

108. Slater, L., & Atekwana, E. (2013). Geophysical signatures of subsurface microbial processes. *Eos, Transactions American Geophysical Union*, *94*(8), 77-78.

109. Slater, L., & Binley, A. (2006). Synthetic and field-based electrical imaging of a zerovalent iron barrier: Implications for monitoring long-term barrier performance. *Geophysics*, *71*(5), B129-B137.

110. Slater LD, & Reeve A (2002) Investigating peatland stratigraphy and hydrogeology using integrated electrical geophysics. Geophysics 67(2):365–378

1085   111.   Slater, L., Binley, A. M., Daily, W., & Johnson, R. (2000). Cross-hole electrical
1086   imaging of a controlled saline tracer injection. *Journal of applied geophysics*, *44*(2-3),
1087   85-102.
1088

1089   112.   Slater, L., Ntarlagiannis, D., Personna, Y. R., & Hubbard, S. (2007). Pore-scale
1090   spectral induced polarization signatures associated with FeS biomineral transformations.
1091   *Geophysical Research Letters*, *34*(21).
1092

1093   113.   Strohmeier, S., Knorr, K. H., Reichert, M., Frei, S., Fleckenstein, J. H., Peiffer,
1094   S., & Matzner, E. (2013). Concentrations and fluxes of dissolved organic carbon in
1095   runoff from a forested catchment: insights from high frequency measurements.
1096   *Biogeosciences*, *10*(2), 905.
1097

1098   114.   Tamura, H., Goto, K., Yotsuyanagi, T., & Nagayama, M. (1974).
1099   Spectrophotometric determination of iron (II) with 1, 10-phenanthroline in the
1100   presence of large amounts of iron (III). *Talanta*, *21*(4), 314-318.
1101

1102

1103   115.   Tsukanov, K., & Schwartz, N. (2020). Relationship between wheat root
1104   properties and its electrical signature using the spectral induced polarization method.
1105   *Vadose Zone Journal*, *19*(1), e20014.
1106

1107   116.   Uhlemann, S.S., Sorensen, J.P.R., House, A.R., Wilkinson, P.B., Roberts, C.,
1108   Gooddy, D.C., Binley, A.M. and Chambers, J.E., 2016. Integrated time-lapse
1109   geoelectrical imaging of wetland hydrological processes. *Water Resources Research*,
1110   *52*(3), pp.1607-1625.
1111

1112   117.   Ulrich, C., & Slater, L. (2004). Induced polarization measurements on
1113   unsaturated, unconsolidated sands. *Geophysics*, *69*(3), 762-771.
1114

1115   118.   Urban, N. R. Retention of sulfur in lake-sediments. in *Environmental Chemistry*
1116   *of Lakes and Reservoirs* (ed. Baker, L. A.) (American Chemical Society, 1994). **237**,
1117   323–369

1118

119.   Vindedahl, A. M., Strehlau, J. H., Arnold, W. A., & Penn, R. L. (2016). Organic matter and iron oxide nanoparticles: aggregation, interactions, and reactivity. *Environmental Science: Nano*, *3*(3), 494-505.

120.   Wainwright, H. M., Flores Orozco, A., Bücker, M., Dafflon, B., Chen, J., Hubbard, S. S., & Williams, K. H. (2016). Hierarchical Bayesian method for mapping biogeochemical hot spots using induced polarization imaging. *Water Resources Research*, *52*(1), 533-551.

121.   Wang, Y., Wang, H., He, J. S., & Feng, X. (2017). Iron-mediated soil carbon response to water-table decline in an alpine wetland. *Nature communications*, *8*(1), 1-9.

122.   Ward, S. H. (1988, January). The resistivity and induced polarization methods. In *Symposium on the Application of Geophysics to Engineering and Environmental Problems 1988* (pp. 109-250). Society of Exploration Geophysicists.

123.   Waxman, M. H., & Smits, L. J. M. (1968). Electrical conductivities in oil-bearing shaly sands. *Society of Petroleum Engineers Journal*, *8*(02), 107-122.

124.   Weigand, M., & Kemna, A. (2017). Multi-frequency electrical impedance tomography as a non-invasive tool to characterize and monitor crop root systems. *Biogeosciences*, *14*(4).

125.   Weller, A., Zhang, Z. and Slater, L., 2015. High-salinity polarization of sandstones. *Geophysics*, *80*(3), pp.D309-D318.

126.   Williams, K. H., Ntarlagiannis, D., Slater, L. D., Dohnalkova, A., Hubbard, S. S., & Banfield, J. F. (2005). Geophysical imaging of stimulated microbial biomineralization. *Environmental science & technology*, *39*(19), 7592-7600.

127.   Williams, K. H., Kemna, A., Wilkins, M. J., Druhan, J., Arntzen, E., N'Guessan, A. L., ... & Banfield, J. F. (2009). Geophysical monitoring of coupled microbial and geochemical processes during stimulated subsurface bioremediation. *Environmental science & technology*, *43*(17), 6717-6723.

128.   Wong, J. (1979). An electrochemical model of the induced-polarization phenomenon in disseminated sulfid ores. *Geophysics*, *44*(7), 1245-1265.

129.   Zhang, C., Ntarlagiannis, D., Slater, L., & Doherty, R. (2010). Monitoring microbial sulfate reduction in porous media using multipurpose electrodes. *Journal of Geophysical Research: Biogeosciences*, *115*(G3).

130.   Zhang, C., Slater, L., & Prodan, C. (2013). Complex dielectric properties of sulfate-reducing bacteria suspensions. *Geomicrobiology Journal*, *30*(6), 490-496.

131.   Zimmermann, E., Kemna, A., Berwix, J., Glaas, W., & Vereecken, H. (2008). EIT measurement system with high phase accuracy for the imaging of spectral induced polarization properties of soils and sediments. *Measurement Science and Technology*, *19*(9), 094010.

132.   Zimmermann, E., Huisman, J. A., Mester, A., & van Waasen, S. (2019). Correction of phase errors due to leakage currents in wideband EIT field measurements on soil and sediments. *Measurement Science and Technology*, *30*(8), 084002.